國立成功大學
太空與電漿科學所
碩士論文

National Cheng Kung University
Institute of Space and Plasma Sciences
Master Thesis

太空與實驗室環境中太陽風與非磁化星球的交互作用之理論研究

Theoretical study of the solar wind interacting with an unmagnetized planet in space and in laboratory

研究生 **(Author):** 葉宜霖 **I-Lin Yeh**

指導老師 **(Advisor):** 張博宇博士 **Dr. Po-Yu Chang**

中華民國一百零八年七月 **July, 2019**

doi:10.6844/NCKU201901460

國立成功大學

碩士論文

太空與實驗室環境中太陽風與非磁化星球的交互作用之理論研究

Theoretical study of the solar wind interacting with an unmagnetized planet in space and in laboratory

研究生：葉宜霖

本論文業經審查及口試合格特此證明

論文考試委員：

呂凌霄

談永頤

張博宇

指導教授：張博宇

系(所)主管：陳炳志

中　華　民　國　108　年　7　月　4　日

摘要

我們正在研究由太陽風與未磁化行星相互作用產生的火星弓形震波 (Martian bow shock)。透過理論研究太陽風的參數，例如太陽風動態壓力和太陽極紫外線通量，如何影響弓形震波的位置，這個課題目前尚未被完全了解。這項理論研究將用於設計我們的實驗室太空科學的實驗，透過國立成功大學太空與電漿科學研究所的6000焦耳的脈衝功率系統來驅動錐形線陣列產生馬赫數高達20的超音速電漿噴流流過障礙物來實現。雖然震波的形成機制在太空和實驗室上有所不同，不過我們透過歐拉相似性的分析證明了在我們未來的實驗中研究火星弓形震波位置是可行的。

我們提出了一個適用於太陽風和非磁化行星之間的相互作用的公式來表達弓形震波鼻子(ionopause nose)的位置，這個公式將用於設計我們未來的實驗。我們用氣體動力學方法計算了弓形震波位置，也就是電離層邊界位置和間隙距離的總和。其中電離層邊界的位置是由壓力平衡公式計算而得的。而弓形震波的間隔距離是由半經驗模型所計算到得到的，其正比於電離層邊界鼻子的曲率半徑。我們最後算出了弓形震波鼻子位置的公式，它取決於電離層的高度尺度，太陽風的動態壓力和電離層的峰值壓力。此外，我們推導出電離層邊界鼻子附近的輪廓方程 (profile equation)。最後我們將我們的理論與氣體動力學模擬和太空儀器量測結果做初步比較，我們的理論結果與模擬和太空儀器量測結果是一致的。

關鍵詞：未磁化行星的弓形震波，對峙距離，氣體動力學理論，電離層，實驗室太空科學，脈衝功率系統

doi:10.6844/NCKU201901460

Abstract

Martian bow shock, the solar wind interacting with the unmagnetized planet, will be studied. We theoretically investigated how the solar parameters, such as solar wind dynamic pressure and solar EUV flux, influences the bow shock location, which is still currently not well understood. This theoretical study will be used to design the laboratory space science experiments. The experiment will be implemented by producing a supersonic plasma jet with Mach number up to 20, which will be generated using a conical wire array, flowing through an obstacle. The conical wire array will be driven by a 6 kJ pulsed-power system in the Institute of Space and Plasma Sciences, National Cheng Kung University, Taiwan. Although the shock formation mechanism is different in space and laboratory condition, we have shown that, through the analysis of the Euler similarity, studying the Martian bow shock location in our potential experiment is feasible.

We present the formula for the location of the bow shock nose for the interaction between the solar wind and unmagnetized planet. This formula will be used to design future experiments. We calculate the bow shock location, the sum of the ionopause location and standoff distance, in the gasdynamics approach. We determine the ionopause nose location using pressure balance formula. The standoff distance of the bow shock is determined by a semiempirical model proportional to the radius of curvature at the ionopause nose. We derived the formula of the shock nose position, which depends upon the scale height in ionosphere, dynamic pressure of the solar wind, and the peak pressure of the ionosphere. Furthermore, we derived the equation of the ionopause profile around the nose. The preliminary comparison of our theory with the results of the gasdynamics simulation and the spacecraft measurement will be presented. Our derived formula is consistent with the simulation and the spacecraft measurement results.

Keywords: bow shock of the unmagnetized planet, standoff distance, ionosphere, gasdynamics theory, laboratory space sciences, pulsed-power system

doi:10.6844/NCKU201901460

致謝

首先我要謝謝博宇老師3年來的指導。老師除了學識淵博外，老師待人處事的態度也很值得學習，每次看到老師都會面帶笑容地回答學生的問題，而且幾乎不會發脾氣。從一開始做模擬到後來做理論，雖然換過很多題目，不過老師總是在一旁給我許多寶貴的建議，也教導了我很多做研究的態度及寫文章的方法，真的很幸運可以遇到老師，非常感謝老師。

再來我要感謝談老師Sunny，還記得我大三來上老師開的太空物理的時候，我十分陶醉於老師的課堂中，老師的理論推導非常嚴謹且清楚，真的讓人感到賞心悦目，每次上課結束後內心總有滿滿的喜悦，也啓發我許多對太空物理的興趣。另外謝謝談老師的高等太空物理中教導我們shock的基本理論，有了老師教導的這些基礎後，我才有辦法進行這份論文研究。

接下來要感謝向老師，你上的課我真的覺得非常享受也感到十分心曠神怡，謝謝你教導許多全世界只有你會教的東西，還有分享很多如何做理論的方法，感到受益良多。除此之外，也因為老師的課，我感受到了理論的強大，進而對電漿理論有更深的興趣。

此外謝謝教導過我的Yas老師，Kawa老師，你們讓我對電漿物理有更深入的了解。還有要感謝所辦的安成及Dabby，謝謝你們引領我進入電漿的世界。

還要感謝實驗室的同學國益, 名城, 知叡, 宛儀及柏維，謝謝你們的陪伴，還有你們常常透過實驗的觀點帶給我許多不一樣的啓發。特別感謝知叡在許多程式上的協助。

最後要謝謝我的家人的支持，有了你們的支持我才能專心完成這份研究。

doi:10.6844/NCKU201901460

Contents

doi:10.6844/NCKU201901460

doi:10.6844/NCKU201901460

List of Tables

doi:10.6844/NCKU201901460

List of Figures

doi:10.6844/NCKU201901460

doi:10.6844/NCKU201901460

doi:10.6844/NCKU201901460

List of Abbreviations and Symbols

c_s	Sound speed after shock
c_o	Sound speed before obstacle (ionopause)
Δ	Standoff distance (the distance between shock nose and the obstacle nose)
ϵ	$=(\gamma-1)/(\gamma+1)$
g	Gravity
γ	Specific heat ratio ($=C_P/C_V$)
H	Ionospheric scale height
k_B	Boltzmann coefficient
k	Reduced coefficient for solar wind dynamic pressure. c.f. Eq. 23
l_{euv}	EUV flux
M_∞	Mach number of the solar wind
M_s	Mach number after shock
P	Thermal pressure
P_{dyn}	Dynamic pressure of the solar wind
$P_{M,i}$	Ionospheric maximal (peak) thermal pressure
P_o	Thermal pressure before obstacle (ionopause)
P_∞	Thermal pressure of the solar wind
P_i	Ionospheric thermal pressure
P_s	Thermal pressure after shock
ψ	Angle between solar wind flow direction and the normal to ionopause
R_o	Radius of curvature of the obstacle (ionopause) nose
$r_{M,i}$	Location of the ionospheric peak pressure
r_o	Location of the obstacle (ionopause) nose
r_s	Location of the shock nose
ρ_∞	Mass density of the solar wind

ρ_s	Mass density after shock
v_s	Velocity after shock
v_∞	Velocity of the solar wind
EUV	Extreme Ultraviolet
UV	Ultraviolet
GPU	Graphics Processing Unit

doi:10.6844/NCKU201901460

1 Introduction

In the nowadays space physics research, more research focuses on the solar wind interacting with the magnetized planet than the unmagnetized planet or weakly-magnetized planet. However, the study of Martian bow shock is recently a hot topic due to the growing interests in the exploration of Mars, a weakly-magnetized planet. Furthermore, more and more data from the spacecraft measurement are available. In order to more detailedly understand the interaction between the solar wind and unmagnetized planet, we plan to simulate this phenomenon in the laboratory experiment driven by a pulsed-power system. A preliminary theoretical model of the bow shock nose position has been derived and will be used for experiment designs.

In section 1.1, we give a brief introduction to the solar wind interacting with the unmagnetized planet. The formation of the Martian bow shock is introduced in section 1.1.1. In section 1.1.2, the previous research on the Martian bow shock location is reviewed. The hydrodynamics boundary condition, which will be used in section 3, will be listed in section 1.1.3. In section 1.2, the goal of this project will be given.

1.1 The interaction between solar wind and unmagnetized planet

There are three types of interaction between the solar wind and an obstacle in space: (1) solar wind interacting with the magnetized obstacle like Earth. (2) solar wind interacting with the unmagnetized obstacle with an atmosphere like Mars and Venus. (3) solar wind interacting with the unmagnetized obstacle without atmosphere like moon. Figure 1 is a schematic of these three types of interaction.

doi:10.6844/NCKU201901460

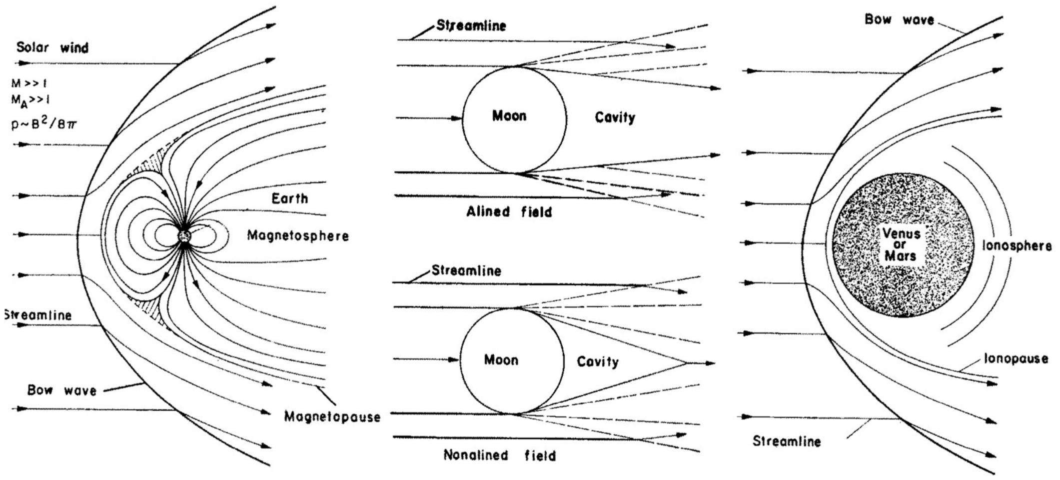

Figure 1: Schematic of solar wind past the (a) Earth (b) Moon (c) Mars and Venus. Courtesy of Ref. [1].

The detached bow shock is formed because of the supersonic solar wind and the deflection of the incident solar wind flow by the magnetosphere or ionosphere. Since the moon has neither ionosphere nor magnetosphere, no bow shock is formed in the solar wind interacting with the moon.

1.1.1 Martian Bow Shock

Formation of the bow shock in plasma interaction with Mars, unmagnetized planets with an atmosphere (Fig. 2), is as follows. First, the ionization by solar EUV radiation in the atmosphere forms an ionospheric obstacle, acting as a conductor. The boundary of the ionosphere is called ionopause. Then the solar-wind plasma with its frozen-in field flows at a supersonic velocity toward the conducting obstacle, resulting in the appearance of the bow shock.

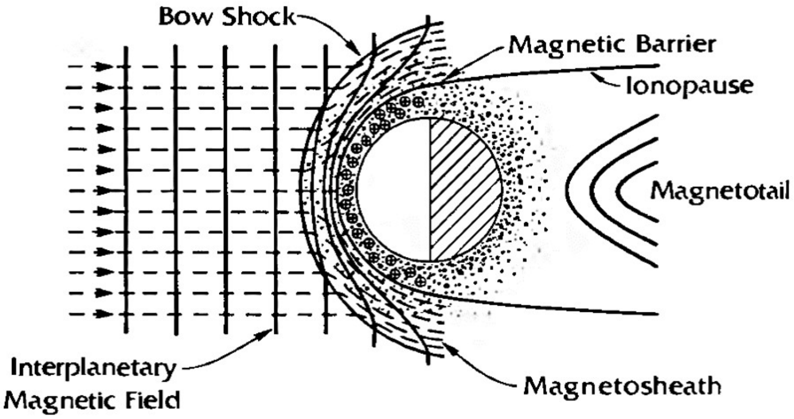

Figure 2: Schematic of the solar wind interaction with an unmagnetized planet with an atmosphere. Courtesy of Ref.[2].

1.1.2 Previous research on the Martian bow shock location

Martian bow shock has been detailedly studied by spacecraft measurement and numerical simulation. Martian bow shock is formed by the interaction between the solar wind and the Martian ionosphere. Recently, the first measurement study[6] of the ionopause from the mission Mars Atmosphere and Volatile EvolutioN (MAVEN, 2014-present) was released in 2015. This mission will provide us a deeper understanding of the Martian bow shock. The shape of the bow shock is often modeled using the least-squares fitting of an axisymmetric or non-axisymmetric conic section[7, 8] with the data from spacecraft measurement. On the other hand, the theoretical model of the planetary bow shock location and shape can be seen in the review paper by Spreiter[9, 1, 10], Slavin[11, 12] and Verigin[13]. An efficient computational model for determining the global properties of the solar wind past a planet based on axisymmetric magnetohydrodynamics was proposed by Spreiter[14]. The specific study of the magnetohydrodynamics simulation for the solar wind interaction with Mars can be seen in Ref.[15] and Ref.[16].

However, it is not well understood how the factors influence the location of the Martian bow shock. The main factors impacting the bow shock position are the solar wind dynamic

doi:10.6844/NCKU201901460

pressure $P_{dyn} = \rho_\infty v_\infty^2$ and solar EUV flux l_{euv}. According to the fitting results (Fig. 3) from the data of Mars Express Analyser of Space Plasma and EneRgetic Atoms (ASPERA-3)[3], it is shown that the bow shock location (r_s) reduces in altitude with increasing solar wind dynamic pressure in the relation $r_s \propto P_{dyn}^{-0.02}$ and increases in altitude with increasing solar EUV flux in the relation $r_s \propto 0.11\, l_{EUV}$. It means that the bow shock position is more sensitive to the solar EUV flux than the solar wind dynamic pressure.

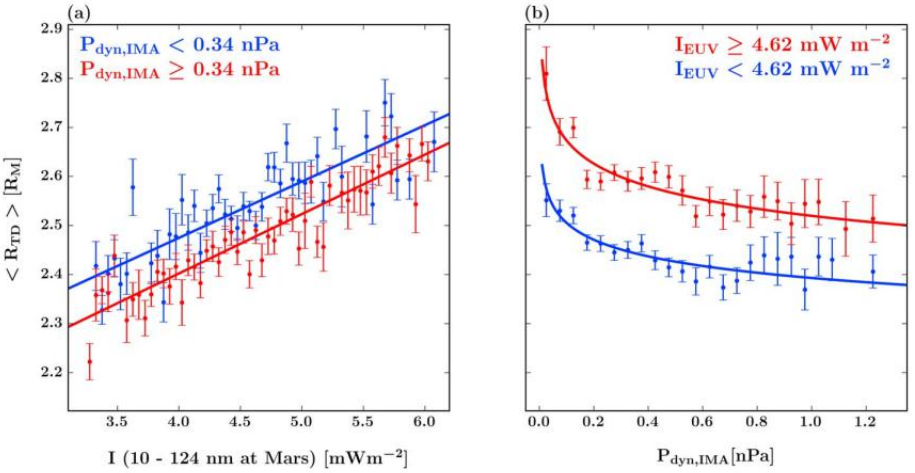

Figure 3: The response of the location of the Martian bow shock with the solar parameters. (a) Bow shock location against solar EUV radiance. (b) Bow shock location against solar wind dynamic pressure. Courtesy of [3].

Other parameters controlling the Martian bow shock location are the intense localized Martian crustal magnetic fields[17], the magnetosonic Mach number[18], the interplanetary magnetic fields and the convective electric field[19]. In this thesis, we will mainly focus on the dependence of the solar wind dynamics pressure and the ionospheric pressure, which is dependent on the solar EUV radiation.

1.1.3 Hydrodynamics boundary condition

Hydrodynamics formulation is used throughout this thesis. Ideal magnetohydrodynamics equations are

$$\begin{aligned}
\frac{\partial \rho}{\partial t} + \nabla \cdot \rho \vec{v} = 0, \\
\rho(\frac{\partial \vec{v}}{\partial t} + \vec{v} \cdot \nabla v) = -\nabla P + \frac{1}{\mu_0}(\nabla \times \vec{B}) \times \vec{B}, \\
\frac{\partial \vec{B}}{\partial t} = \nabla \times \vec{v} \times \vec{B}, \\
\frac{\partial P}{\partial t} + \vec{v} \cdot \nabla P = -\gamma\, P\, \nabla \cdot \vec{v},
\end{aligned} \tag{1}$$

where p is the pressure, ρ is the mass density, $\vec{v}$ is the velocity and $\vec{B}$ is the magnetic field. The first one is the continuity equation, the second is the momentum equation, the third is Faraday's law and the last is the entropy conservation equation, or adiabatic equation. Here we assume the gas follows the polytropic condition and adiabatic process.

magnetohydrodynamics equations can be reduced to hydrodynamics equations under the condition that the magnetic pressure term is much smaller than the thermal pressure term in the right-hand side of the momentum equation (second equation in Eq. 1)

$$|\frac{\frac{1}{\mu_0}(\nabla \times \vec{B}) \times \vec{B}}{\nabla P}| \approx \frac{B^2/2\mu_0}{P} = 1/\beta, \tag{2}$$

where plasma beta β is defined as thermal pressure divided by magnetic pressure. For the condition of solar wind past the unmagnetized planet, β is much larger than 1 in both space and laboratory, so we can neglect the force term containing the magnetic field in the momentum equation, reducing the magnetohydrodynamics formulation to pure

doi:10.6844/NCKU201901460

hydrodynamics formulation

$$
\begin{aligned}
\frac{\partial \rho}{\partial t} + \nabla \cdot \rho\, \vec{v} = 0, \\
\rho(\frac{\partial \vec{v}}{\partial t} + \vec{v} \cdot \nabla v) = -\nabla p, \\
\frac{\partial P}{\partial t} + \vec{v} \cdot \nabla P = -\gamma\, P\, \nabla \cdot \vec{v}.
\end{aligned} \tag{3}
$$

Throughout the thesis, we will use hydrodynamics formulation instead of magnetohydrodynamics due to the high beta condition. The first one is the mass conservation equation, the second is the momentum equation for ideal fluid, or Euler equation and the third is the adiabatic equation.

The boundary condition for steady-state ideal hydrodynamics[5] is

$$
\begin{aligned}
[\rho v_n] = 0 \\
\left[P + \rho v_n^2\right] = 0 \\
[\rho v_n \vec{v_t}] = 0 \\
\left[v_n(\frac{\rho v^2}{2} + \frac{\gamma\, P}{\gamma - 1})\right] = 0,
\end{aligned} \tag{4}
$$

where the subscript n and t are the normal direction and tangential direction, respectively. The brackets mean the difference of the quantity between both sides of the boundary. The Eq. 4 indicates the continuity of the mass flux, momentum flux and energy flux. Note that the discontinuity surfaces of the ionopause and the bow shock are zero thickness under the description of the dissipationless ideal (magneto)hydrodynamics[5, 20].

In our study, we are interested in two types of boundary:

doi:10.6844/NCKU201901460

- Tangential discontinuity[5, 9, 1] at the ionopause

$$\begin{aligned}[\rho] &\neq 0\\ [\vec{v_t}] &\neq 0\\ v_n &= 0\\ [P] &= 0.\end{aligned} \tag{5}$$

The normal velocity is zero in the tangential discontinuity. We will utilize the continuity of the thermal pressure to determine the location and the radius of curvature at the ionopause nose. Furthermore, we can observe that there is a density jump across the ionopause according to tangential discontinuity.

- Shock waves[5, 9, 1] at the bow shock front

$$\begin{aligned}[\rho v_n] &= 0\\ [\vec{v_t}] &= 0\\ \left[P + \rho v_n^2\right] &= 0\\ \left[\frac{v_n^2}{2} + \frac{\gamma\, P/\rho}{\gamma - 1}\right] &= 0.\end{aligned} \tag{6}$$

For our purpose of the study of the global phenomenon like bow shock position, the ideal fluid description is enough. We are not going to study microphysics such as the shock formation mechanism, so the dissipation process of the shock will not be discussed throughout the thesis. In general, the shock in the laboratory is formed in a collisional environment without magnetic field; the shock in the space is formed in a collisionless magnetized environment and the shock dissipation mechanism is the wave-particle interaction.

1.2 The goal of the project

Martian bow shock, the solar wind interaction with the unmagnetized planet, will be studied in laboratory conditions using a 6 kJ pulsed-power system in Institute of Space and Plasma Sciences, National Cheng Kung University, Taiwan. The experiment will be implemented by generating a supersonic plasma flow with Mach number up to 20 using a conical wire array flowing through an obstacle. Since it is not well understood how the location of the Martian bow shock is influenced by the solar parameters such as solar wind dynamic pressure and EUV flux, we plan to investigate it in both theory and the laboratory experiment.

In this thesis work, we study the location of the bow shock generated from the interaction between the solar wind and unmagnetized planet in the theoretical aspect. The formula for the shock nose location as a function of the solar wind dynamic pressure and EUV flux will be presented and compared with the spacecraft measurement. This theoretical results will be used for our future experiment designs. Past studies by others are all related to observation, but this study is related to both laboratory experiment and observation. On the other hand, we are not going to study fine structure in the transition region of a shock and the shock microphysics, even though it is more theoretically fascinating. The dissipation mechanism for the shock will not influence the location of the bow shock, so we use the ideal hydrodynamics formulation throughout this work. Note that the thickness of the discontinuity surface is zero under the ideal hydrodynamics description.

Some numerical works will also be presented in this theses. In our initial phase of studying the Martian bow shock, we planned to investigate it through numerical simulation. A 1D particle-in-cell simulation for two-stream instability has been done for learning numerical skills, which is shown in Appendix C. We set up a GPU-accelerated particle-in-cell simulation in the cluster in our laboratory (Appendix D) as well. However, we after that switched to the theoretical study since we realized that, for experiment design, the

doi:10.6844/NCKU201901460

theoretical formula is more useful than the numerical simulation. The analytical theory is essential for machine designing because the relationship between each physical quantities can be known in the formula. However, in simulation, to know the results from different conditions requires different runs, which is very numerically intensive especially for multi-scale and multi-physics simulation.

In this thesis, we will focus on theoretically determining the location of the nose of the bow shock for the solar wind past the unmagnetized planet. The formula for shock nose location is developed and compared to the results from the spacecraft measurement. Laboratory space science is the other topic in this thesis. The theoretical results will be used for the optimization of the experimental designs. In Chapter 2, we will introduce the concept of the laboratory space sciences and our experiment system. In Chapter 3, we will give a detailed derivation of the formula for the shock nose position. The comparison of our formula and the spacecraft measurement results will be shown in the last section of Chapter 3. In Chapter 4, we will show the application of our formula to experiment designs for our system. In Chapter 5, we will discuss future works. In Chapter 6, the conclusion of the thesis will be given.

doi:10.6844/NCKU201901460

2 Laboratory Space Sciences

Laboratory experiments provide a complement understanding of space physics without the limitations from the spacecraft measurement.[21] Experiments overcome the restriction that the spacecraft measurements are made only at one point in space. Furthermore, laboratory experiments have the advantage of greater control of plasma condition, enabling the reproducible experiments, less expensive than the spacecraft launching. The principle of the laboratory space sciences is based on the similarity of (magneto)hydrodynamics.[22, 23]

In section 2.1, we introduce the concept of the scaling relation and Euler similarity. In section 2.2, the introduction of the plasma jet produced using conical-wire array driven by our pulsed power system will be given. In section 2.3, we discuss the space and laboratory condition for the similarity analysis.

2.1 Scaling relation and similarity criteria

We discuss the conditions under which the two systems will have identical behavior, with the assumption that they are both ideal fluid (with zero viscosity and heat conductivity)[22]. The governing equations for the ideal fluid are mass continuity equation, Euler equation, and adiabatic equation, as shown in the following equations

$$\begin{aligned} \frac{\partial \rho}{\partial t} + \nabla \cdot \rho\,\vec{v} = 0, \\ \rho(\frac{\partial \vec{v}}{\partial t} + \vec{v} \cdot \nabla v) = -\nabla P, \\ \frac{\partial P}{\partial t} + \vec{v} \cdot \nabla P = -\gamma\, P\, \nabla \cdot \vec{v}. \end{aligned} \tag{7}$$

All governing equations of the ideal fluid remain unchanged under the transformation that

$$\vec{r_1} = a\vec{r_2}, \quad \rho_1 = b\rho_2, \quad P_1 = cP_2, \quad t = a\sqrt{\frac{b}{c}}t_2, \quad \vec{v_1} = \sqrt{\frac{c}{b}}\vec{v_2}, \tag{8}$$

where a, b, c are arbitrary positive constants and the subscripts 1 and 2 mean the physical quantities of system 1 and system 2.

Consider the initial-value problem in an ideal hydrodynamics system 1 with the following initial conditions

$$\rho_1(t=0) = \tilde{\rho_1}\, f(\vec{r_1}/L_1), \quad P_1(t=0) = \tilde{P}_1\, g(\vec{r_1}/L_1), \quad \vec{v_1}(t=0) = \tilde{v}_1\, \vec{h}(\vec{r_1}/L_1), \tag{9}$$

where the L_1, $\tilde{\rho_1}, \tilde{p}_1$, $\tilde{v}_1$ are the characteristic length, mass density, pressure, velocity, respectively, of the system 1 and f, g, $\vec{h}$ are dimensionless function. And the initial condition for the system 2 is

$$\rho_2(t=0) = \tilde{\rho_2}\, f(\vec{r_2}/L_2), \quad P_2(t=0) = \tilde{P}_2\, g(\vec{r_2}/L_2), \quad \vec{v_2}(t=0) = \tilde{v_2}\, \vec{h}(\vec{r_2}/L_2), \tag{10}$$

where the L_2, $\tilde{\rho_2}, \tilde{p_2}$, $\tilde{v_2}$ are the characteristic length, mass density, pressure, velocity, respectively, of the system 2. According to the last equation in Eq. 8, we can get

$$\vec{v_1} = \sqrt{\frac{P_1/P_2}{\rho_1/\rho_2}}\vec{v_2}. \tag{11}$$

By expressing p, ρ and $\vec{v}$ in terms of the characteristic quantities in Eq. 9 and Eq. 10, then Eq. 11 can be written as

$$\tilde{v_1}\sqrt{\frac{\tilde{\rho}_1}{\tilde{p_1}}} = \tilde{v_2}\sqrt{\frac{\tilde{\rho}_2}{\tilde{p_2}}}. \tag{12}$$

We can conclude that the transformation in Eq. 8 holds if two systems both have the same value of Euler number, that is, $Eu = \tilde{v}(\tilde{\rho}/\tilde{P})^{1/2}$. This similarity is called the Euler similarity[22] since it is derived from the Euler equation. If the system is described by the ideal magnetohydrodynamics equations, then Euler similarity can be modified to Euler-Alfven similarity[23], which includes one more condition $B/\sqrt{p}$ to follow besides the Euler number.

Thus, in the condition of the ideal hydrodynamics fluid, two systems behave identically if the initial conditions are geometrically similar and the Euler number ($Eu = \tilde{v}(\tilde{\rho}/\tilde{P})^{1/2}$) in both systems are the same. The second system will evolve identically on a time scale $\tilde{\tau_2} = \tilde{\tau_1}\frac{\tilde{L_2}}{\tilde{L_1}}\sqrt{(\tilde{P_1}/\tilde{\rho_1})/(\tilde{P_2}/\tilde{\rho_2})}$ according to Eq. 8.

Since the hydrodynamics similarity is based on the ideal fluid equation, the underlying assumptions of the ideal fluid must be followed when using the Euler similarity:

1. The dissipative process is negligible (though the shock is allowed to be present):

    (a) The system is required to be collisional. The localization has to occur on the length scale that is much smaller than the characteristic length of the problem L. It is required $r_{Li} \ll L$ or $l_c \ll L$, where r_{Li} is the ion Larmor radius and l_c is the collision mean free path. The condition is either

    $$\frac{r_{Li}}{L} \simeq 10^{-4}\frac{v(cm/s)}{B(G)L(cm)} \ll 1 \tag{13}$$

    or

    $$\frac{l_c}{L} \simeq 3\times 10^{13}\frac{T^2(eV)}{\Lambda\, L(cm)\, n_i(1/cm^3)} \ll 1, \tag{14}$$

    where Λ is the Coulomb logarithm and the expression of the mean free path is from Braginskii[24].

    (b) Viscous dissipation should be insignificant. It requires that viscous force is much smaller than the inertial force, that is, Reynolds number much larger

doi:10.6844/NCKU201901460

than 1. The condition is

$$Re = \frac{L\,v}{\nu} \gg 1, \tag{15}$$

where ν is the kinematic viscosity. The detailed evaluation of the Reynolds number for Euler similarity can be seen in Ref.[22].

(c) Energy flow by particle heat conduction should be negligible. It means that the heat advection is much more important than the heat conduction, i.e., Peclet number much larger than 1. The detailed evaluation of the Peclet number for Euler similarity can be seen in Ref.[22].

(d) Energy flow by radiation flux should be negligible. That is, the hydrodynamics energy fluxes must be much larger than the radiation energy flux, i.e., radiative Peclet number is much larger than 1. The detailed evaluation of radiative Peclet number can be seen in Ref.[22].

2. Gas in both systems should be polytropic, that is, the internal energy is proportional to the pressure, and have the same adiabatic constant γ.

3. Magnetic field effect on the motions of the gas is neglected. In other words, the magnetic pressure is assumed to be much less than the gas pressure. If the magnetic field effect is important, we can use Euler-Alfven similarity[23].

Euler similarity breaks down at spatial scales much less than the global scale when dissipative processes become important. The existence of the transport coefficient such as viscosity and thermal diffusivity will break the similarity transformation.

2.2 Introduction to our experiment system

We plan to simulate the solar wind interacting with an unmagnetized planet in the laboratory. The solar wind is simulated by the plasma jet generated by the conical-wire

doi:10.6844/NCKU201901460

array. The experiment is driven by the home-made pulsed power system.

2.2.1 Pulsed-power system

We use a parallel plate capacitor bank (PPCB) for our pulsed-power system (Fig. 4). The system is being built from scratch and will start being operated by July 2019. The pulsed-power system can generate a very high current in an extremely short period. The PPCB contains twenty 1 μF capacitors, two rail-gap switches, one coaxial transmission line, two parallel plate transmission lines and a cylindrical vacuum chamber oriented vertically.

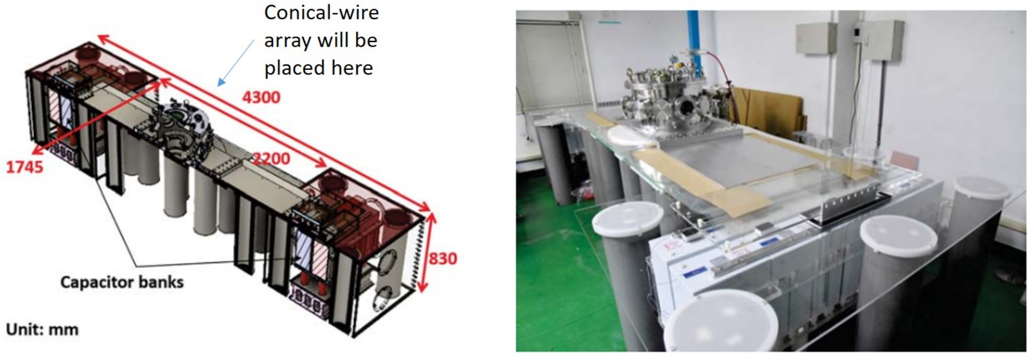

Figure 4: Schematic and photo of our pulsed-power system using a parallel plate capacitor bank (PPCB).

The estimated parameters of our pulsed-power system are shown in Table 1. In July 2019, we plan to start to operate our pulsed power system, which can be charged to $\sim$ 20 kV. delivering a current of $\sim$ 120 kA. In the near future, we target to make the system fully functional at 50 kV, providing a peak current of $\sim$ 300 kA and power of 4 GW.

Capacitance	5 μF
$\mathrm{V}_{\mathrm{change}}$	20 / 50 kV
Energy	1 / 6.25 kJ
$\mathrm{I}_{\mathrm{peak}}$	$\sim 120/\sim 300$kA
Rise time	$\sim 1.3\mu s$
Power	$\sim 0.8/\sim 4\,$GW

Table 1: Summaries of the expected parameters of our pulsed-power system. The values in the left sides are the estimated value we can achieve in July 2019 and the values in the right sides are the value of the ultimate goal which can be achieved in the near future.

2.2.2 Conical-wire arrays

Conical-wire arrays (Fig. 5) will be used to generate a supersonic plasma jet for simulating solar wind. When a high current, which is generated via our pulsed-power system, passes through a conical array, wires are heated and ionized because of the ohmic heating. The current also generates a global azimuthal magnetic field $\vec{B_A}$ at the same time. Thus, the plasma at the wires is pinched by the $J \times B$ force. The pinch effect happens faster near the cathode than the anode since the radius of the wire array at the cathode is smaller than that near the anode. Thus, a supersonic plasma jet propagating from the cathode toward anode is generated. This plasma jet is generally unmagnetized, but it can be magnetized by embedding a pair of magnets in the system. As for simulating the planetary ionosphere in the laboratory, we can use the UV light to illuminate the gas around obstacle forming a simulated ionosphere.

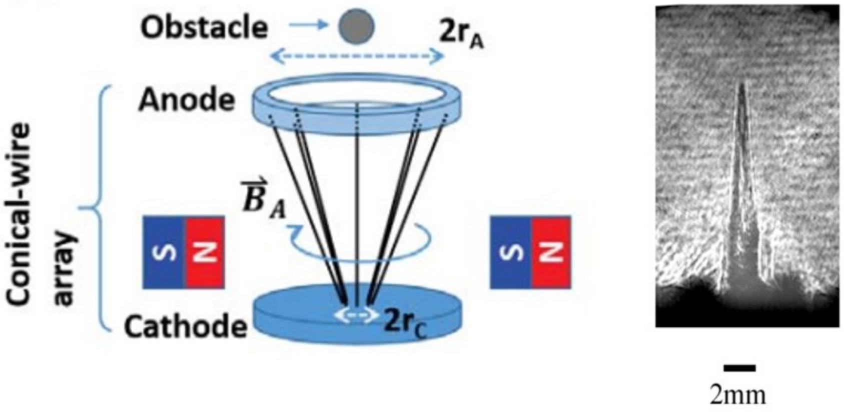

Figure 5: Conical-wire array will b used to generate a plasma jet. The right one is the Schlieren image of the plasma jet generated by the group in Imperial College London[4].

Though we have not started operating the system, we estimate that the plasma jet generated by conical arrays driven by the pulsed-power system will produce the jet with the sonic Mach number up to 30 referred to the previous experiments done by the group in Imperial College London[4]. According to the Euler similarity we introduced in the previous section, two different systems will behave identically if they have the same Euler number ($Eu = \tilde{v}(\tilde{\rho}/\tilde{p})^{1/2}$), which can be approximated by Mach number. Therefore, we justify that we can simulate the solar wind interacting with the unmagnetized planet in our laboratory experiment because the Mach number of our system and the solar wind are approximately same. The detailed comparison of the parameters in our system and space environment can be seen in section 2.3.

2.3 Our potential experiment and scaling relation

In this section, we detailedly analyze the parameters in the space and the laboratory experiment. Since our pulsed power system is still being built, the estimated value of the characteristic parameters for our lab experiment is referred to the experiment done by the group in Imperial College London[4], which also utilizes the conical-wire array driven by the pulsed power system. The value of the characteristic parameters for the solar wind interacting with Mars can be seen in the paper by Slavin[11].

The characteristic parameters for space and the laboratory condition is shown in Table 2. For the parameters in space in the table, “Length scale” is the Mars diameter, “Drive velocity” is the solar wind speed, “Mass density” is the mass density in the solar wind near the Mars, “Temperature” is the proton temperature in the solar wind near the Mars, “Magnetic field” is the interplanetary magnetic field near the Mars. Note that the space environment is collisionless so that the temperature equilibration is not effective. The electron temperature of the solar wind near the Mars is 13 eV. For the laboratory condition, the electron and the ion temperature is the almost same since the plasma is in the collisional environment.

Item	Symbol	Value in space	Estimated value in lab
Length scale (cm)	L	7×10^8	10^{-2}
Drive velocity (km/s)	v	430	200
Timescale (s)	L/v	16.1	5×10^{-10}
Mass density (g/cm^3)	ρ	5×10^{-24}	10^{-3}
Pressure (dyn/cm^2)	P	2.5×10^{-11}	8×10^8
Temperature (eV)	T	6.1	50
Magnetic field (nT)	B	3.3	N/A
Euler number	$\mathrm{v}\sqrt{\rho/\mathrm{P}}$	19	22
Magnetic localization	$\mathrm{r_{L,i}/L}$	0.2	N/A
Collisional localization	$\mathrm{l_c/L}$	1.4×10^3	10^{-4}

Table 2: Characteristic parameters in space environment and the laboratory condition.

According to the Table 2, the Euler number in the space and laboratory environment is at the same order. The Reynolds number and the Peclet number of the plasma jet in the laboratory experiment are much larger than 1 ($\mathrm{Re} > 10^4$, $\mathrm{Pe} > 10$) [4], the dissipative process can be neglected. The length scale is very large in space, so the Peclet number and Reynolds number can be regarded as much larger than 1, i.e., the dissipative process is negligible. As for the localization, the particles in space and laboratory is localized by the magnetic field and collision, respectively. Thus, we can conclude that the two systems

doi:10.6844/NCKU201901460

will behave identically based on the Euler similarity, which we described in section 2.1.

doi:10.6844/NCKU201901460

3 Determination of the location of the bow shock nose

We theoretically investigate the bow shock location as a function of the solar wind and the ionospheric conditions, such as solar wind dynamic pressure $\rho_\infty v_\infty^2$, ionospheric scale length H, ionospheric peak pressure $P_{M,i}$ and the location of the ionospheric peak pressure $r_{M,i}$. The equation of bow shock location is derived and will be used to design the future experiments. We only focus on the nose location of the bow shock but not the whole shape profile of the bow shock. The shape of the bow shock and the ionopause is assumed to be symmetric around the x-axis.

The schematic of the bow shock and the obstacle boundary (ionopause) is shown in the Fig. 6. We use the following symbols to represent the geophysical quantities in the report: r_o is nose positions of the obstacle, r_s is nose positions of the bow shock, $r_{M,i}$ is the location inside ionosphere where maximal thermal pressure occurs, Δ is the bow shock standoff distance, i.e., the distance between ionopause nose position and bow shock nose position.

doi:10.6844/NCKU201901460

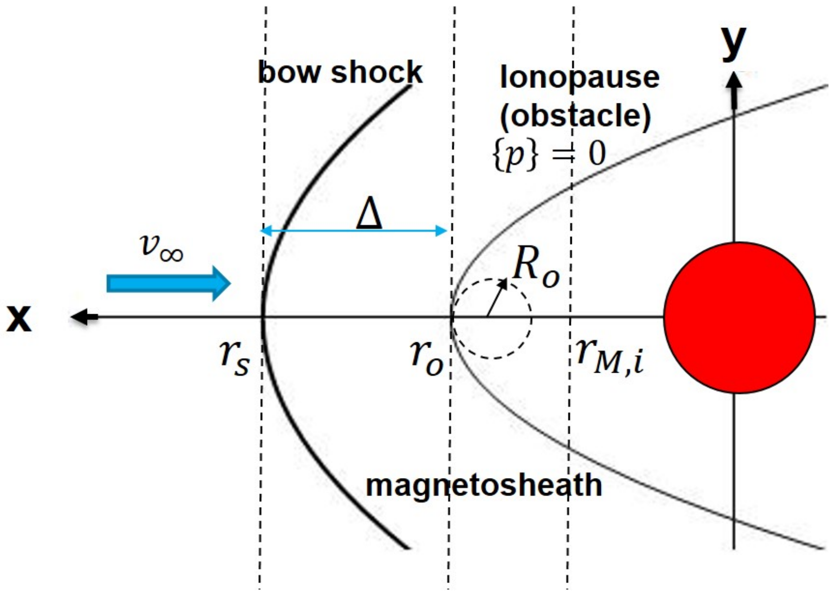

Figure 6: Definition of each variable used in the report

The goal is to determine the shock nose location r_s:

$$r_s = r_o + \Delta. \tag{16}$$

Ionopause nose location r_o is calculated using the continuity of the thermal pressure by tangential discontinuity[9, 1, 13]; bow shock standoff distance is calculated by the empirical formula[7, 13].

The derivation of the ionopause nose location and the radius of curvature at ionopause nose are in subsection 3.2. The standoff distance formula is introduced in subsection 3.3. Finally, the formula of the bow shock nose location is shown in section 3.4. The comparison of the theory and the observation results will be given in section 3.5.

3.1 Overview of the theory

In this section, we have an overview of all the theories which are used for calculating the location of the bow shock nose in terms of the solar wind and the ionospheric conditions.

doi:10.6844/NCKU201901460

Fig. 7 shows the variation of the thermal pressure along the stagnation streamline.

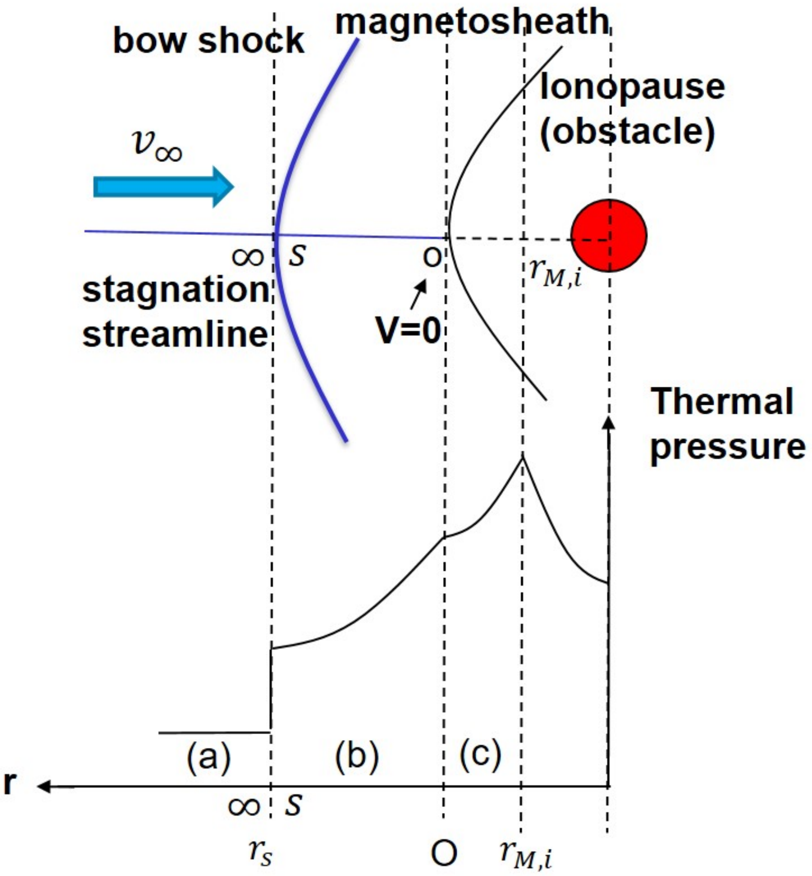

Figure 7: Thermal pressure along the stagnation streamline.

- (a) Solar wind
  - In the region of the solar wind, the thermal pressure can be expressed as a function of the dynamic pressure and the sonic Mach number, i.e., $P_\infty = \rho_\infty v_\infty^2/(M_\infty^2\gamma)$.
- (a) – (b) Bow shock
  - At the bow shock, momentum flux conservation in the normal shock relation is used

$$P_\infty + \rho_\infty v_\infty^2 = P_s + \rho_s v_s^2. \tag{17}$$

Note that the entropy increases across the shock.

- (b) Magnetosheath
  - Within the magnetosheath, the plasma follows the process of the isentropic compression, i.e., the combination of the energy conservation of the compressible flow (Bernoulli equation)

    $$\frac{2\gamma}{\gamma - 1} P + \rho\, v^2 = \text{constant}, \tag{18}$$

    and the adiabatic relation

    $$P\, V^\gamma = \text{constant}, \tag{19}$$

    where V is the volume. We can observe that the sum of the thermal pressure and the dynamic pressure is conserved before and after shock, but not conserved along the stagnation streamline within the magnetosheath. Therefore, the value of $P + \rho v^2$ before shock is not the same as that at stagnation point.
- (b)-(c) Ionopause
  - At the ionopause, the thermal pressure is continuous according to tangential discontinuity.
- (c) Upper ionosphere
  - Within the upper ionosphere, the hydrostatic equilibrium (the balance between the gravity force and the pressure gradient) is assumed.

doi:10.6844/NCKU201901460

3.2 Ionopause (obstacle boundary)

Ionopause, the boundary of the ionosphere, is the location of the thermal pressure balance according to tangential discontinuity.[1, 13]. We first investigate the pressure variation on the center line, then the ionopause nose location r_o and the radii of curvature at the ionopause nose R_o.

3.2.1 Thermal pressure at the ionopause

Ionopause profile is determined by the thermal pressure continuity at both sides of the ionopause according to tangential discontinuity. Here we discuss the thermal pressure at both sides of the ionopause respectively.

- Thermal pressure at the inner side of the ionopause

  The thermal pressure in the ionosphere is assumed to be spherical symmetric and at hydrostatic equilibrium[1] in equivalence to the balance between pressure gradient and gravity force. The detailed derivation of the hydrostatic equilibrium can be seen in Appendix A. So the thermal pressure inside the ionosphere can be expressed as

  $$P_i(r) = P_{M,i}\exp(\frac{r_{M,i}-r}{H}), \tag{20}$$

  where $P_i(r)$ is the pressure inside the ionosphere, $r_{M,i}$ is the location inside ionosphere where peak thermal pressure $P_{M,i}$ occurs and $H = k_BT/mg$ is the scale height in which $m = 1.67\times10^{-24}g$ is the mass for a singly ionized hydrogen, k_B is Boltzmann's constant and T is the absolute temperature for plasma and assumed to be constant inside the ionosphere.

- Thermal pressure at the outer side of the ionopause

  We use Rayleigh pitot tube formula[5, 9, 15] to obtain the thermal pressure just

doi:10.6844/NCKU201901460

outside the ionosphere as a function of the solar wind dynamic pressure. Rayleigh pitot tube formula is used for the stagnation pressure at the blunt body nose with a detached bow shock. It is derived in two steps: (1) applying the hydrodynamic normal shock jump condition to get the downstream thermal pressure; (2) applying the isentropic compression to determine the thermal pressure at the stagnation point with Bernoulli's law on the stagnation streamline within the magnetosheath. The rigorous derivation is shown in Appendix B. The Rayleigh pitot tube formula is given as

$$P_o = P_\infty M_\infty^2 (\frac{\gamma+1}{2})^{(\gamma+1)/(\gamma-1)} \frac{1}{[\gamma-(\gamma-1)/(2M_\infty^2)]^{1/(\gamma-1)}}, \tag{21}$$

where P_o is the thermal pressure at the ionopause nose, P_∞ is the thermal pressure of the solar wind, M_∞ is the sonic Mach number of the solar wind and γ is the specific heat ratio. Then, we plug $M_\infty = \frac{v_\infty}{\sqrt{\gamma p_\infty/\rho_\infty}}$ into the Rayleigh pitot tube formula, the relationship between thermal pressure at the ionopause P_o as a function of solar wind dynamic pressure $\rho_\infty v_\infty^2$ can be expressed as

$$P_o = k\rho_\infty v_\infty^2, \tag{22}$$

where

$$k = (\frac{\gamma+1}{2})^{(\gamma+1)/(\gamma-1)} \frac{1}{\gamma\,[\gamma-(\gamma-1)/(2M_\infty^2)]^{1/(\gamma-1)}}. \tag{23}$$

For $\gamma = 5/3$ and $M_\infty \gg 1$, this relation can be simplified to $k = 0.88$.

3.2.2 Nose position of the ionopause r_o

The formula of the ionopause nose position r_o is determined by the thermal pressure continuity at the ionopause according to tangential discontinuity:

$$P_o = P_i(r_o). \tag{24}$$

doi:10.6844/NCKU201901460

Fig. 8 is the schematic of the pressure balance between ionosphere pressure and solar wind pressure.

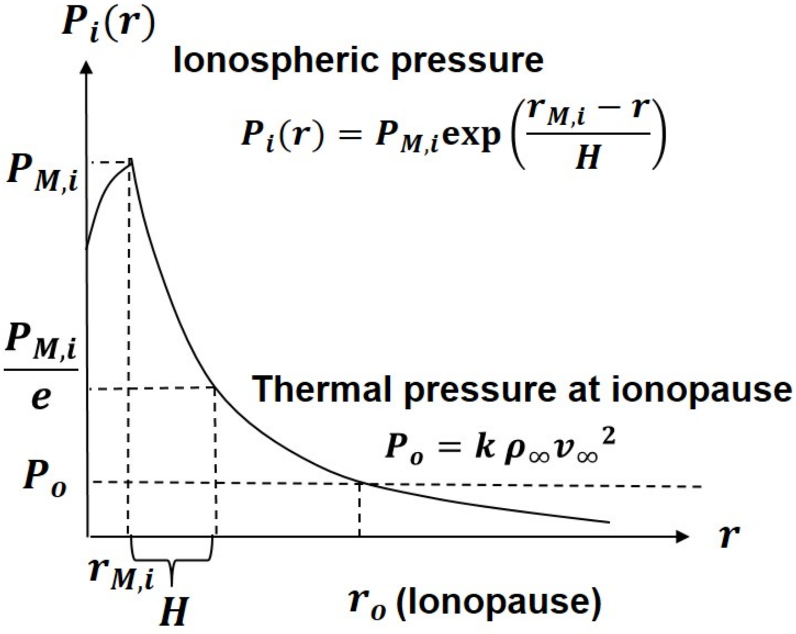

Figure 8: The schematic of the pressure balance between the solar wind pressure and ionosphere pressure

By solving Eq. 24 with the expression of the thermal pressure at the both side of the ionopause (Eq. 20 and Eq. 22), the formula of the nose position of the bow shock r_o can be derived as

$$r_o = r_{M,i} + H\ \ln(\frac{P_{M,i}}{k\rho_\infty v_\infty^2}). \tag{25}$$

The derived equation of the nose position (Eq. 25) of the ionopause is reasonable: the shorter the scale height H or the larger the dynamic pressure of the solar wind $\rho_\infty v_\infty^2$, then ionopause closer to planet surface.

3.2.3 Radius of curvature at ionopause nose R_o

In this section, we analytically calculate the radius of curvature at ionopause nose R_o by solving the ionopause profile equation near the ionopause nose. Since the ionopause

doi:10.6844/NCKU201901460

is symmetric at x-axis, the ionopause profile can be expressed as $x = x(y)$. We do the Taylor expansion at $y = 0$ of the ionopause profile $x = x(y)$, then we can get the equation of the ionopause profile at the vicinity of the ionopause nose

$$x(y) = x(0) + (y - 0)\,x'(0) + \frac{1}{2}(y - 0)^2 x"(0) + ... \tag{26}$$

Note that on the ionopause profile, $x(0) = r_o$ and $x'(0) = 0$. Furthermore, by the definition of the radius of curvature $R(y) = |\frac{(1+x'(y))^{3/2}}{x"(y)}|$, the radius of curvature at ionopause nose ($y = 0$) can be written as $R_o = -1/x"(0)$. Thus, the equation of the ionopause profile near the ionopause nose can be reduced to a quadratic equation

$$x = r_o - \frac{1}{2R_o}y^2. \tag{27}$$

Here we neglect the third and higher order term of the Taylor expansion.

The whole ionopause profile can be determined by the thermal pressure continuity at the ionopause according to tangential discontinuity, that is, the thermal pressure is equal at the outer side and the inner side of the ionopause.

$$k\rho_\infty v_\infty^2 \cos^2\psi = P_i(r), \tag{28}$$

where ψ is the angle between v_∞ and the normal to ionopause, which is shown in Fig. 9.

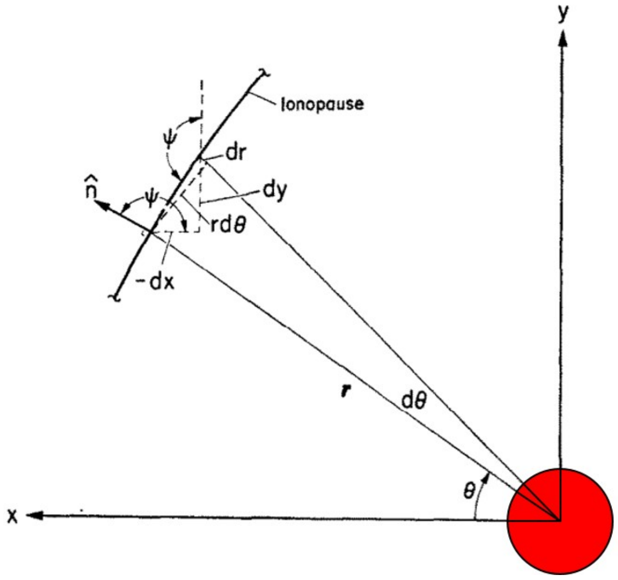

Figure 9: Element of the ionopause and the coordinate. Modified figure from Ref. [1].

The left hand side of the equation is the thermal pressure approximated at the outer side of the ionopause deviated from the nose position and the right hand side is the ionospheric pressure we introduced in section 3.2.1. Since $k\rho_\infty v_\infty^2$ is the ionospheric pressure at the ionopause nose $P_i(r_o)$, the equation of the ionopause profile (Eq.28) can be reduced to

$$P_i(r_o)\cos^2\psi = P_i(r). \tag{29}$$

By the geometric relation, $cos^2\psi$ can be expressed as

$$cos^2\psi = \left(\frac{dy}{ds}\right)^2 = \frac{(r\,d\theta\,\cos\theta + dr\,\sin\theta)^2}{dr^2 + (r\,d\theta)^2}. \tag{30}$$

We substitute the cosine relation in Eq.30 into the pressure continuity equation at the ionopause (Eq.29), we get

$$P_i(r_o)\frac{\left(\cos\theta + (\frac{dr}{r\,d\theta})\sin\theta\right)^2}{\left(\frac{dr}{r\,d\theta}\right)^2 + 1} = P_i(r). \tag{31}$$

doi:10.6844/NCKU201901460

Then we solve for $dr/r\,d\theta$ to obtain

$$\frac{dr}{r\,d\theta} = \frac{-P_i(r_o)\sin 2\theta + 2\sqrt{P_i(r)P_i(r_o) - P_i^2(r)}}{2(P_i(r_o)\sin^2\theta - P_i(r))}. \tag{32}$$

This is the differential equation for the ionopause profile, which can be solved numerically[1] with the initial condition $r\,(\theta = 0) = r_o$. Note that the ionopause is symmetric about the $x = 0$ axis ($\theta = 0$), so the first-order derivative at the ionopause nose is zero, that is,

$$\frac{1}{r(0)}\frac{dr}{d\theta}(0) = \frac{1}{r_o}\frac{dr}{d\theta}(0) = 0. \tag{33}$$

In the second term of the numerator in the ionospause profile differential equation (Eq.32), it contains a square root. The value of the quantity inside the square root must be equal or larger than zero, or the square root term will become imiginary, which is physically unallowable. So, we can get

$$P_i(r)P_i(r_o) - P_i^2(r) \geq 0, \tag{34}$$

where $P_i(r)$ is the ionospheric pressure exponentially decaying outward because of hydrostatic equilibrium. Then we can obtain that the ionopause profile must follow the condition

$$r \geq r_o. \tag{35}$$

The equalitity occurs at the ionopause nose.

For our purpose of deriving the radius of curvature at the ionopause nose, we only have to focus on the vicinity of the ionopause nose, i.e., the region $\theta \rightarrow 0$ and $r \rightarrow r_o$. Furthermore, at the ionospause nose, $dr/rd\theta$ can be approximated by dx/dy. The differential equation for the ionopause profile (Eq. 32) at the vicinity of the ionopause nose can be simplified to

doi:10.6844/NCKU201901460

$$
\begin{aligned}
\frac{dx}{dy} &= -\sqrt{\frac{P_i(r_o)}{P_i(r)} - 1} \\
&= -\sqrt{\frac{P_i(r_o)}{P_i(r)}}\sqrt{1 - \frac{P_i(r)}{P_i(r_o)}} \\
&\simeq -\sqrt{1 - \frac{P_i(r)}{P_i(r_o)}}.
\end{aligned} \tag{36}
$$

Now we express $P_i(r)$ in Taylor series at $r = r_o$, then the right hand side of the Eq. 36 can be rewritten as

$$
\begin{aligned}
-\sqrt{1 - \frac{P_i(r)}{P_i(r_o)}} &= -\sqrt{-(r - r_o)\frac{P_i'(r_o)}{P_i(r_o)} - \frac{1}{2}(r - r_o)^2\frac{P_i''(r_o)}{P_i(r_o)} - ...} \\
&= -\sqrt{-(r - r_o)\frac{P_i'(r_o)}{P_i(r_o)}}\sqrt{1 + \frac{1}{2}(r - r_o)\frac{P_i''(r_o)}{P_i'(r_o)} + ...} \\
&\simeq -\sqrt{-(r - r_o)\frac{P_i'(r_o)}{P_i(r_o)}}\left(1 + \frac{1}{4}(r - r_o)\frac{P_i''(r_o)}{P_i'(r_o)} + ...\right).
\end{aligned} \tag{37}
$$

Thus, now the differential equation for the ionopause profile near the ionopause nose is

$$
\frac{dx}{dy} = -\sqrt{-(r - r_o)\frac{P_i'(r_o)}{P_i(r_o)}}\left(1 + \frac{1}{4}(r - r_o)\frac{P_i''(r_o)}{P_i'(r_o)} + ...\right) \tag{38}
$$

Also, by $x \rightarrow r_o$and $y \rightarrow 0$ at the vicinity of the ionopause nose, $r - r_o$ can be approximated by

doi:10.6844/NCKU201901460

$$\begin{aligned}
r - r_o &= \sqrt{x^2 + y^2} - r_o \\
&= \sqrt{\left[r_o + (x - r_o)\right]^2 + y^2} - r_o \\
&= \sqrt{r_o^2 + 2\,r_o(x - r_o) + (x - r_o)^2 + y^2} - r_o \qquad (39) \\
&= r_o\sqrt{1 + 2\,\frac{x - r_o}{r_o} + \frac{(x - r_o)^2}{r_o^2} + \frac{y^2}{r_o^2}} - r_o \\
&\simeq r_o\left(1 + \frac{x - r_o}{r_o} + \frac{(x - r_o)^2}{2\,r_o^2} + \frac{y^2}{2\,r_o^2}\right) - r_o \qquad (40) \\
&= x - r_o + \frac{(x - r_o)^2}{2\,r_o} + \frac{y^2}{2\,r_o}. \qquad (41)
\end{aligned}$$

By substituting the equation of the ionopause profile near the ionopause nose (Eq.27) in to Eq.41, we get

$$\begin{aligned}
r - r_o &= -\frac{1}{2R_o}y^2 + \frac{\left(-\frac{1}{2R_o}y^2\right)^2}{2\,r_o} + \frac{y^2}{2\,r_o} \qquad (42) \\
&\simeq \frac{y^2}{2}\left(\frac{1}{r_o} - \frac{1}{R_o}\right) \qquad (43)
\end{aligned}$$

In Eq.42, the second term at the right hand side is negligible as $y \to 0$ since it is of the order y^4 and the other two terms are of the order y^2.

We plug the $r - r_o$ relation (Eq. 43) into the differential equation of the ionopause profile (Eq. 38), then integrate the differential equation

$$\int_{r_o}^{x} dx = -\int_0^y dy \sqrt{\frac{-1}{2}\frac{P_i'(r_o)}{P_i(r_o)}\left(\frac{1}{r_o} - \frac{1}{R_o}\right)}\left(y + \frac{1}{8}\left(\frac{1}{r_o} - \frac{1}{R_o}\right)\frac{P_i''(r_o)}{P_i'(r_o)}\,y^3 + ...\right). \qquad (44)$$

Therefore we obtain the formula of the ionopause profile at the vicinity of the ionopause:

$$x = r_o - \sqrt{-\frac{P_i'(r_o)}{2P_i(r_o)}\left(\frac{1}{r_o} - \frac{1}{R_o}\right)}\left(\frac{y^2}{2} + \frac{1}{32}\left(\frac{1}{r_o} - \frac{1}{R_o}\right)\frac{P_i''(r_o)}{P_i'(r_o)}\,y^4 + ...\right). \qquad (45)$$

By comparing Eq. 45 and Eq. 27, finally, we get the equation of the radius of curvature at the ionopause nose

$$R_o = \sqrt{-\frac{2P_i(r_o)}{P_i'(r_o)}\frac{R_o r_o}{R_o - r_o}}. \tag{46}$$

Eq.46 can be rearranged as a quadratic equation

$$R_o^2 - r_o\,R_o - \sqrt{-\frac{2P_i(r_o)}{P_i'(r_o)}}\,r_o = 0. \tag{47}$$

Then we solve it and get

$$R_o = \frac{r_o \pm \sqrt{r_o^2 + 4\sqrt{-\frac{2P_i(r_o)}{P_i'(r_o)}}\,r_o}}{2}. \tag{48}$$

We take the plus sign in the nominator since R_o will be negative if we take the minus sign, which is not physically allowable. Thus, we obtain the expression of the radius of curvature at the ionopause nose

$$R_o = \frac{r_o + \sqrt{r_o^2 + 4\sqrt{-\frac{2P_i(r_o)}{P_i'(r_o)}}\,r_o}}{2}. \tag{49}$$

With the ionospheric pressure $P_i(r)$ of the form in Eq. 20, the radius of curvature at the ionopause nose can be expressed as

$$R_o = \frac{r_o + \sqrt{r_o^2 + 8\,H\,r_o}}{2}, \tag{50}$$

where H is the scale height of the ionosphere. The expression of the radius of curvature at the ionopause nose from our calculation is the same as that from the Table A1 in Verigin *et al.* (2003) [13]. Thus, by plugging Eq.50 into Eq.27, we can get the ionopause profile

doi:10.6844/NCKU201901460

near the ionopause nose

$$x = r_o - \frac{1}{r_o + \sqrt{r_o^2 + 8\,H\,r_o}}\,y^2. \tag{51}$$

In the derivation of the radius of curvature at the ionopause nose and the ionopause profile near the ionopause nose, we made many assumptions to get it. We have shown that the assumption we made above is all valid by verifying our analytical results with the simulation results, which will be given in Section 3.5.1.

This equation of the radius of the curvature at the ionopause (Eq.50) tells that

$$R_o \geq r_o. \tag{52}$$

The equality occurs as the ionospheric scale height H is close to zero. By the equation of the ionopause nose location (Eq.25), we get that r_o is equal to $r_{M,i}$ when H is zero. Combining the above relation, we found that

$$R_o \to r_{M,i} \text{ as H} \to 0. \tag{53}$$

This relation means that if the ionospheric pressure decreases very sharply outward, the radius of the ionopause nose is about the distance between the location of the ionospheric peak pressure and the planet center. Furthermore, we can observe that R_o is smaller as the dynamic pressure of the solar wind is larger since r_o is smaller. These results are physically reasonable.

3.3 Bow shock standoff distance Δ

The standoff distance of the bow shock Δ is determined by the empirical model [9, 7, 13, 25]. This empirical model is supported by gasdynamics experiment and observations

doi:10.6844/NCKU201901460

of the flow past the planets[12]. The standoff distance is expressed by the empirical model

$$\frac{\Delta}{R_o} = 0.87\frac{\rho_\infty}{\rho_s}, \tag{54}$$

where $\rho_\infty$and ρ_s are the mass density before and after shock, respectively and 0.87 is the empirical coefficient. The bow shock nose is farther from the obstacle as the radius of curvature of the obstacle nose is larger (Fig. 10). Bow shock can touch the obstacle only when the leading end of the obstacle is pointed.

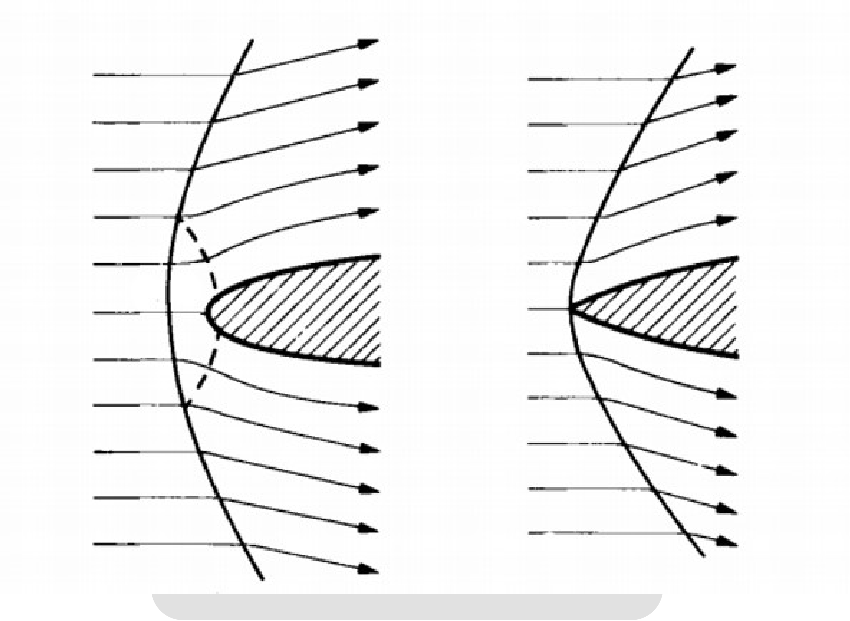

Figure 10: Schematic of the detached shock. Courtesy of [5]

The density ratio across the shock is related to solar wind Mach number and the specific heat ratio

$$\frac{\rho_\infty}{\rho_s} = \frac{(\gamma - 1)M_\infty^2 + 2}{(\gamma + 1)M_\infty^2}. \tag{55}$$

Thus, in the condition of the solar wind Mach number much larger than 1, the standoff distance can be expressed as

$$\Delta = 0.87\ R_o\epsilon, \quad M_\infty \gg 1, \tag{56}$$

doi:10.6844/NCKU201901460

where $\epsilon = \frac{\gamma-1}{\gamma+1}$. By substituting the Eq. 50 into Eq. 56, we get

$$\begin{aligned} \Delta &= 0.87\epsilon \frac{r_o + \sqrt{r_o^2 + 8\,H\,r_o}}{2}, \quad M_\infty \gg 1, \qquad (57) \\ &= r_o\,0.435\,\epsilon \left(1 + \sqrt{1 + 8\,H/r_o}\right), \quad M_\infty \gg 1. \end{aligned}$$

According to this relation, we can obtain the value of the standoff distance if we have the ratio of H (scale height of the ionosphere) to r_o (the distance between ionopause and the center of the planet).

3.4 The formula of the bow shock nose location

Thus, combining the results above, the shock nose location can be written as

$$\begin{aligned} r_s &= r_o + \Delta, \qquad (58) \\ &= r_o + 0.435\,\epsilon \left(r_o + \sqrt{r_o^2 + 8\,H\,r_o}\right), \quad M_\infty \gg 1, \end{aligned}$$

where

$$r_o = r_{M,i} + H\ \ln\left(\frac{P_{M,i}}{k\rho_\infty v_\infty^2}\right), \qquad (59)$$

, scale height $H = k_B T/(mg)$ and $\epsilon = \frac{\gamma-1}{\gamma+1}$.

Note that this equation is only valid for the sonic Mach number of the solar wind much larger than 1. As we can see in the shock nose equation (Eq. 58): the shorter the scale height H or the larger the dynamic pressure of the solar wind $\rho_\infty v_\infty^2$, bow shock nose is closer to the planet. This result is reasonable and intuitive.

3.5 Comparison with the numerical simulation and spacecraft measurement results

The comparison of our formula of the bow shock location with the numerical simulation and the spacecraft measurement results is given in this section.

3.5.1 Verification of the analytical form of the radius of curvature by simulation

In this section, we verify the analytical results of the radius of curvature from the Section 3.2.3 by the numerical simulation. In our calculation, we analytically solve the differential equation of the ionopause profile

$$\frac{dr}{r\,d\theta} = \frac{-P_i(r_o)\sin 2\theta + 2\sqrt{P_i(r)P_i(r_o) - P_i^2(r)}}{2(P_i(r_o)\sin^2\theta - P_i(r))} \tag{60}$$

near the ionopause nose ($\theta \to 0$) with the initial condition $r\,(\theta = 0) = r_o$ to the get the equation of the ionopause profile near the ionopause nose

$$x = r_o - \frac{1}{r_o + \sqrt{r_o^2 + 8\,H\,r_o}}\,y^2. \tag{61}$$

The radius of curvature at the ionopause nose can be obtained as

$$R_o = \frac{r_o + \sqrt{r_o^2 + 8\,H\,r_o}}{2}. \tag{62}$$

In the derivation of the equation of the ionopause profile near the ionopause nose and the radius of curvature at the ionopause nose, we made many assumptions, so we will verify that the assumptions are valid by numerical simulation.

We use the function *NDSolve* in the software *Mathematica* to solve the differential equation of the ionopause profile (Eq.60) to get the ionopause profile $r = r(\theta)$. We

doi:10.6844/NCKU201901460

first compare the numerical result with our analytical result of the ionopause profile near the ionopause nose (Eq.61). Fig.11 shows the comparison of the ionopause profile from analytical theory and numerical simulation. We can observe that, from both the simulation and analytical results, the ionopause follows the rule that

$$r \geq r_o, \tag{63}$$

which we show in the section 3.2.3. Also, we can see that the ionopause profile from analytical theory and numerical simulation match well near the nose position ($y \to 0$), which is reasonable since the analytical result is calculated under the approximation that $\theta \to 0$ in polar coordinate or $y \to 0$ in cartesian cooridinate.

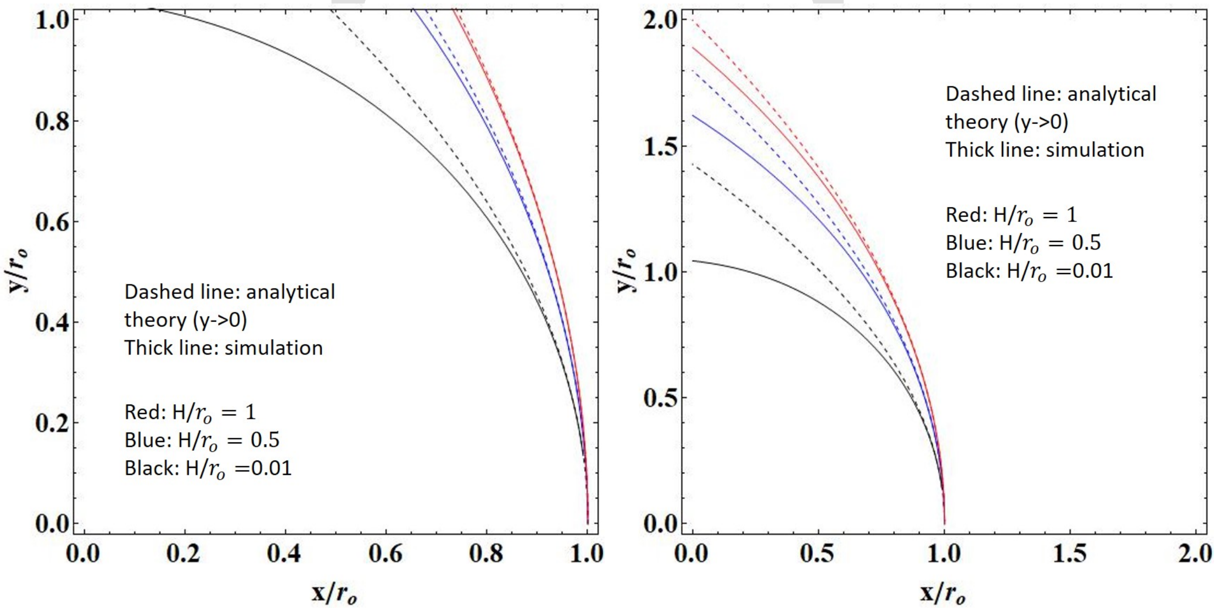

Figure 11: Ionopause profile calculated from analytical theory (Eq.61) and numerical simulation. The left and the right panel have the plot range $[0, r_o]$ and $[0, 2\,r_o]$, respectively. The analytical results is calculated under the approximation that $\theta \to 0$ in polar coordinate or $y \to 0$ in cartesian coordinate.

We then compare the numerical results with our analytical result of the radius of curvature at the ionopause nose (Eq.62). In the numerical simulation, we numerically

doi:10.6844/NCKU201901460

solve the differential equation of the ionopause profile (Eq.60) to get the ionopause profile $r = r(\theta)$ using the function *NDSolve* in *Mathematica* and then calculate the radius of curvature at $\theta = 0$ in polar coordinate using the formula

$$R(\theta) = \frac{\left(r^2(\theta) + r'^2(\theta)\right)^{3/2}}{\left|r^2(\theta) + 2\, r'^2(\theta) - r(\theta) r''(\theta)\right|}. \tag{64}$$

The comparison results are shown in Fig.12. The percentage error of our analytical results compared to the numerical results is defined as (analytical result - numerical result)/numerical result×100. We can see that the percentage error of our analytical results is smaller than 1 percent. Thus, our analytical form of the radius of curvature at the ionopause nose (Eq.62) is verified. And we can say that the assumptions we made in the derivation are valid.

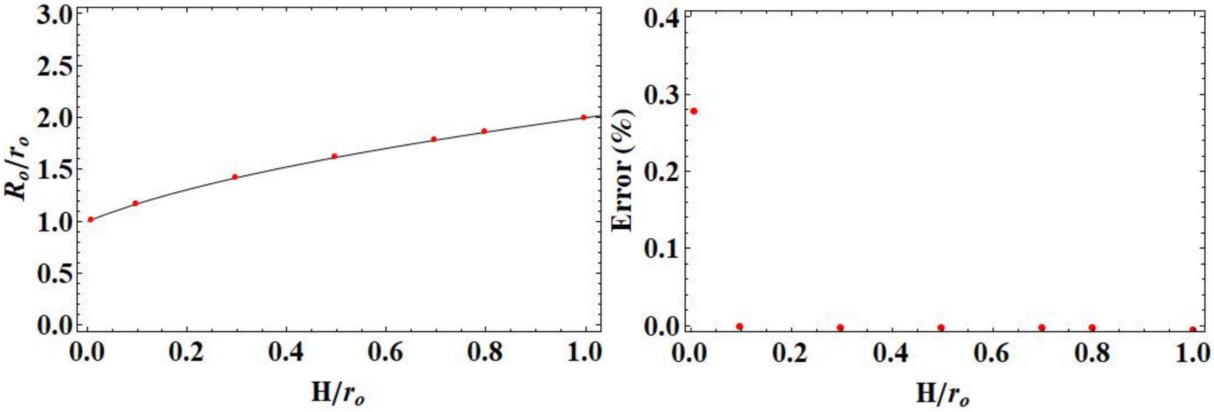

Figure 12: Radius of curvature at the ionopause nose from analytical theory (Eq.62) and numerical simulation. In the left panel, the thick line is the analytical theory (Eq.62) and the red dots are simulation results. In the right panel, it shows the percentage error, which is defined as (analytical result - numerical result)/numerical result×100. The cases with $H/r_o = 0.01$, 0.1, 0.3, 0.5, 0.7, 0.8, 1.0 are considered.

3.5.2 Comparison with hydrodynamics simulation

We now want to compare our formula of the bow shock nose with the simulation and spacecraft measurement results. Our derived formula of the bow shock location is

$$r_s = r_o + r_o\, 0.435\, \frac{\gamma - 1}{\gamma + 1} \left(1 + \sqrt{1 + 8\, H/r_o}\right), \quad M_\infty \gg 1, \tag{65}$$

and the standoff distance is

$$\Delta = r_o\, 0.435\, \frac{\gamma - 1}{\gamma + 1} \left(1 + \sqrt{1 + 8\, H/r_o}\right), \quad M_\infty \gg 1. \tag{66}$$

The nonlinear gasdynamics simulation result for the bow shock profile is referred to the paper by Spreiter *et al.*, 1970[1], which is shown in Fig. 13.

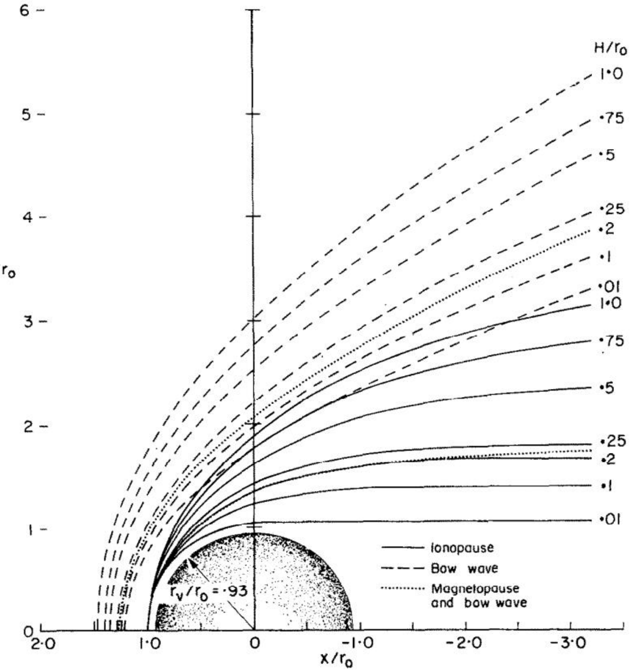

Figure 13: Gasdynamics simulation results for the locations of the bow shock and ionopause with different H/r_o for $M_\infty = 8$ and $\gamma = 5/3$. Courtesy of Spreiter *et al.*, (1970) [1].

In Fig. 14, we compare our formula of the standoff distance with the simulation results

doi:10.6844/NCKU201901460

from Fig. 13.

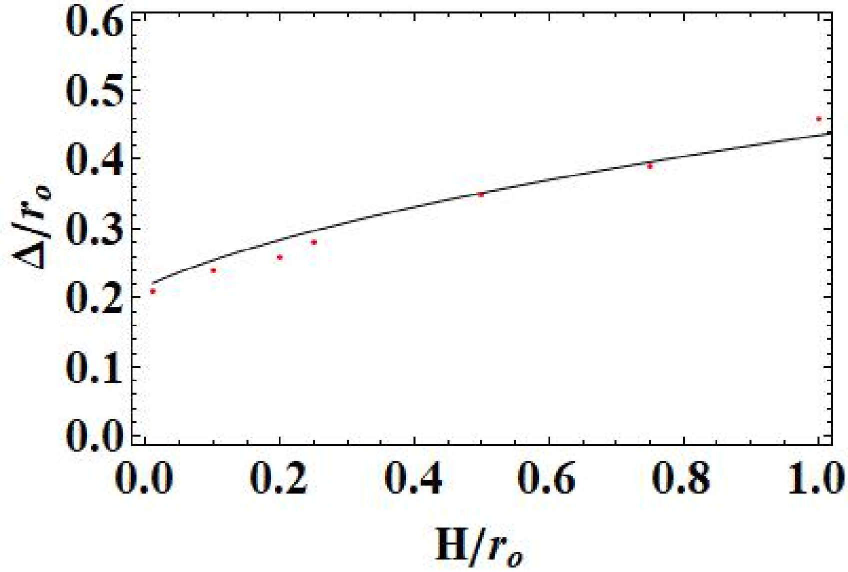

Figure 14: Comparison of the derived standoff distance formula (Eq. 66) with the gasdynamics simulation results from *Spreiter et al.*, 1970[1]. The red dots are the simulation results; the black line is Eq. 66. The cases with $H/r_o = 0.01$, 0.1, 0.2, 0.25, 0.5, 0.75, 1.0 are considered.

As we can observe in the comparison, our derived formula (Eq. 66) and the simulation results match well and both show that the standoff distance becomes larger with the increasing scale heights of the ionosphere. We can conclude that the theory is validated by the simulation results. Note that this formula of the bow shock standoff distance is only applied for the solar wind interacting with the unmangetized planet and the Mach number of the solar wind solar wind must be much larger than 1. The other assumption in this theory is that the ionosphere of the unmagnetized planet is in hydrostatic condition, resulting in the thermal pressure exponentially decaying outward.

3.5.3 Comparison with spacecraft measurements

We investigate the influence of the shock location from solar parameters, which control the P_{dyn} (dynamic pressure of the solar wind), $P_{M,i}$ (peak pressure of the ionosphere),

doi:10.6844/NCKU201901460

$H = k_B T/mg$ (scale height of the ionosphere). Our derived formula of the shock nose location is

$$r_{s}. = r_o + r_o\, 0.435\, \frac{\gamma - 1}{\gamma + 1} \left(1 + \sqrt{1 + 8\, H/r_o}\right), \quad M_\infty \gg 1, \tag{67}$$

where

$$r_o = r_{M,i} + H\ \ln(\frac{P_{M,i}}{k\rho_\infty v_\infty^2}). \tag{68}$$

We are interested in how the variation of the solar parameters influence the shock nose location. The third term can be neglected in the variation study since it contains the square root. So we can obtain that

$$r_s \propto H \ln\left(\frac{P_{M,i}}{k\, P_{dyn}}\right). \tag{69}$$

According to the spacecraft measurement[6], which we introduce in section 1.1.2, the measurement data shows that the bow shock location increases linearly with the increasing EUV flux, but it reduces through a power law relationship with solar wind dynamic pressure,

$$r_s \propto p_{dyn}^{-0.02}\ and\ r_s \propto 0.11\, l_{EUV}. \tag{70}$$

The increasing solar EUV flux will cause the $P_{M,i}$ (peak pressure of the ionosphere) increase via increasing the ionization rate. Furthermore, the increasing solar EUV flux will let the temperature increase, i.e., a larger scale height H. The detailed relation how the variation of the EUV flux influence the peak pressure of the ionosphere $P_{M,i}$ and ionospheric scale height H will be investigated in the future.

We can observe that our relation in Eq. 69 and the spacecraft measurement results in Eq. 70 both shows that the increasing solar EUV flux and decreasing solar wind dynamic pressure will increase the bow shock location. Since the dynamics pressure P_{dyn} term is in the logarithm in our relation in Eq. 69, we suggest that the variation of dynamics pressure has less impact on the shock location than the EUV flux, which controls the scale height H and ionospheric peak pressure $P_{M,i}$. Thus, we can conclude that our derived formula is qualitatively consistent with the spacecraft measurement results that the shock nose location is more sensitive to the solar EUV flux than solar wind dynamics pressure.

doi:10.6844/NCKU201901460

4 Experiment designs

We will simulate the Martian bow shock phenomenon in our laboratory experiment. However, In the laboratory experiment, the condition of hydrostatic equilibrium from gravity can not be produced due to the lack of enough gravity. To simulate the ionosphere in the laboratory, a high power UV LED or a spark driven by a small pulsed-power generator will be used to produce UV light. We will use the UV light to illuminate the obstacle to let the gas around the obstacle be ionized, forming a simulated ionosphere. An artificial ionosphere with plasma pressure exponentially decaying outward is expected to be generated. The supersonic plasma jet is produced using the conical-wire array device, as introduced in section 2.2. The schematic of our potential laboratory experiment for studying the solar wind interacting with the unmagnetized planet is shown in Fig. 15.

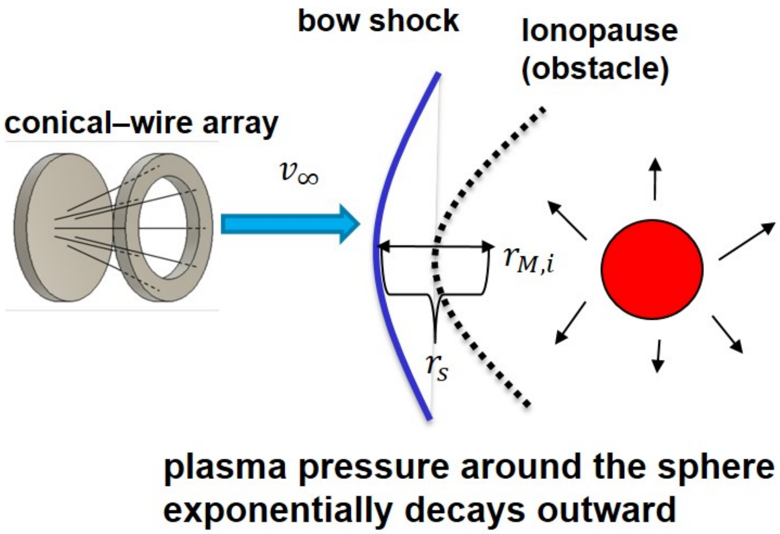

Figure 15: A schematic of our potential experiment.

The formula of the shock nose equation is

$$r_s = r_o + r_o\, 0.435\, \frac{\gamma - 1}{\gamma + 1} \left(1 + \sqrt{1 + 8\, H/r_o}\right), \quad M_\infty \gg 1, \tag{71}$$

where

$$r_o = r_{M,i} + H \ \ln(\frac{P_{M,i}}{k\rho_\infty v_\infty^2}), \tag{72}$$

scale height $H = k_B T/(mg)$ and $\epsilon = \frac{\gamma-1}{\gamma+1}$. It will be used to design our future experiments. The variables in the experiment for this formula are:

- Plasma jet: ρ_∞ and v_∞
- Ionosphere: $r_{M,i}$, H and $P_{M,i}$

In our potential experiment, the scale height can be obtained by fitting the experiment data; other variables can be directly measured in the experiment. We will expect there will be two density jump in the experiment: one is the bow shock front according to the shock discontinuity and the other is the ionopause according to the tangential discontinuity.

doi:10.6844/NCKU201901460

5 Future works

1. **Investigate how the solar EUV radiance influences the ionospheric density and temperature:**

   In order to have a more thorough comparison of our theory with the measurement results, we have to study how the solar EUV flux controls the ionospheric pressure. The textbook edited by Kivelson & Russell (1995)[2] provides some detailed contexts about photoionization from EUV radiation.

2. **Investigate the influence of the interplanetary magnetic field on the location of the bow shock**:

   Throughout the thesis, we neglect the effect of the magnetic field for simplicity. In fact, Mars has some local magnetic field, which can influence the bow shock nose location. The magnetic field also influences the formation mechanisms of the bow shock and the ionopause. In the realistic condition, the interaction between the interplanetary magnetic field and the ionosphere will generate the "induced magnetosphere" and "magnetic pile-up boundary". Furthermore, the magnetic draping effect will occur. The more illustration of these concepts from the magnetic field can be seen in the textbook by Russell *et al.* (2016)[26]. We would like to further study the effect of the magnetic field.

3. **Investigate the impact of the different constituents of the ionosphere on the scale height:**

   In the Martian atmosphere, there are many different constituents like ionized hydrogen, helium, oxygen and carbon dioxide. The scale height (k_BT/mg) is controlled by the constituents of the ionosphere. Thus, the different constituents will make a difference on the bow shock location.

4. **Investigate the assumption that the temperature is constant in the iono-**

doi:10.6844/NCKU201901460

sphere:

In the derivation of the ionospheric pressure formula, we assume the temperature is constant with altitude. However, in the real condition, the temperature varies with the altitude. So, the validity of this assumption requires further investigation.

doi:10.6844/NCKU201901460

6 Conclusion

It is not well understood how the solar parameters influence the location of the Martian bow shock. The location of the bow shock produced from the solar wind interacting with the unmagnetized planet has been theoretically investigated since we want to investigate the interaction between the solar wind and the unmagnetized planet through laboratory experiment in the future. The device of the conical-wire array driven by a pulsed power system is used to generate the plasma jet for simulating the solar wind. To see whether we can simulate this phenomenon in the laboratory experiment, we compare the parameters of the condition in laboratory and space. The comparison results show that the study of the Martian bow shock location is doable since the Euler number ($v\sqrt{\rho/p}$) of both system is very close.

The formula for the location of the bow shock produced from the solar wind interacting with the unmagnetized planet is presented. The bow shock location is the sum of the ionopause location and standoff distance. The whole calculation is based on the gasdynamics formulation since the magnetic effect can be neglected in both space and laboratory condition. We determine the ionopause nose location using pressure balance formula. The standoff distance of the bow shock produced by the supersonic plasma jet around an obstacle is determined by an empirical model. The formula of the shock nose position was derived and showed that the shock nose location increases with the increasing scale height of ionosphere, the decreasing dynamic pressure of the solar wind and the increasing peak pressure of the ionosphere. Our derived formula is qualitatively consistent with the results from spacecraft measurement and the gasdynamics simulations. A more thorough comparison of our theory with the simulation and the spacecraft measurement will be made in the future. This theoretical result will be useful for designing future experiments for studying the location of the Martian bow shock.

doi:10.6844/NCKU201901460

References

[1] John R Spreiter, Audrey L Summers, and Arthur W Rizzi. Solar wind flow past nonmagnetic planets—venus and mars. *Planetary and Space Science*, 18(9):1281–1299, 1970.

[2] Christopher T. Russell Margaret G. Kivelson, editor. *Introduction to space physics.* Cambridge university press, 1995.

[3] Benjamin Edward Stanley Hall, Mark Lester, Beatriz Sánchez-Cano, Jonathan D Nichols, David J Andrews, Niklas JT Edberg, Hermann J Opgenoorth, Markus Fränz, M Holmström, Robin Ramstad, et al. Annual variations in the martian bow shock location as observed by the mars express mission. *Journal of Geophysical Research: Space Physics*, 121(11):11–474, 2016.

[4] SV Lebedev, JP Chittenden, FN Beg, SN Bland, A Ciardi, D Ampleford, S Hughes, MG Haines, A Frank, EG Blackman, et al. Laboratory astrophysics and collimated stellar outflows: The production of radiatively cooled hypersonic plasma jets. *The Astrophysical Journal*, 564(1):113, 2002.

[5] Lev Davidovich Landau and EM Lifshiëtís. *Fluid mechanics.* Butterworth-Heinemann,, 1987.

[6] Marissa F Vogt, Paul Withers, Paul R Mahaffy, Mehdi Benna, Meredith K Elrod, Jasper S Halekas, John EP Connerney, Jared R Espley, David L Mitchell, Christian Mazelle, et al. Ionopause-like density gradients in the martian ionosphere: A first look with maven. *Geophysical Research Letters*, 42(21):8885–8893, 2015.

[7] MH Farris and CT Russell. Determining the standoff distance of the bow shock: Mach number dependence and use of models. *Journal of Geophysical Research: Space Physics*, 99(A9):17681–17689, 1994.

doi:10.6844/NCKU201901460

[8] JG Trotignon, C Mazelle, C Bertucci, and MH Acuna. Martian shock and magnetic pile-up boundary positions and shapes determined from the phobos 2 and mars global surveyor data sets. *Planetary and Space Science*, 54(4):357–369, 2006.

[9] John R Spreiter, Audrey L Summers, and Alberta Y Alksne. Hydromagnetic flow around the magnetosphere. *Planetary and Space Science*, 14(3):223–253, 1966.

[10] John R Spreiter and SS Stahara. The location of planetary bow shocks: A critical overview of theory and observations. *Advances in Space Research*, 15(8-9):433–449, 1995.

[11] James A Slavin and Robert E Holzer. Solar wind flow about the terrestrial planets 1. modeling bow shock position and shape. *Journal of Geophysical Research: Space Physics*, 86(A13):11401–11418, 1981.

[12] JA Slavin, RE Holzer, JR Spreiter, SS Stahara, and DS Chaussee. Solar wind flow about the terrestrial planets: 2. comparison with gas dynamic theory and implications for solar-planetary interactions. *Journal of Geophysical Research: Space Physics*, 88(A1):19–35, 1983.

[13] M Verigin, J Slavin, A Szabo, T Gombosi, G Kotova, O Plochova, K Szegö, M Tátrallyay, K Kabin, and F Shugaev. Planetary bow shocks: Gasdynamic analytic approach. *Journal of Geophysical Research: Space Physics*, 108(A8), 2003.

[14] John R Spreiter and Stephen S Stahara. A new predictive model for determining solar wind-terrestrial planet interactions. *Journal of Geophysical Research: Space Physics*, 85(A12):6769–6777, 1980.

[15] John R Spreiter and Stephen S Stahara. Computer modeling of solar wind interaction with venus and mars. *Washington DC American Geophysical Union Geophysical Monograph Series*, 66:345–383, 1992.

doi:10.6844/NCKU201901460

[16] Yingjuan Ma, Andrew F Nagy, Kenneth C Hansen, Darren L DeZeeuw, Tamas I Gombosi, and KG Powell. Three-dimensional multispecies mhd studies of the solar wind interaction with mars in the presence of crustal fields. *Journal of Geophysical Research: Space Physics*, 107(A10):SMP–6, 2002.

[17] D Vignes, MH Acuña, JEP Connerney, DH Crider, H Reme, and C Mazelle. Factors controlling the location of the bow shock at mars. *Geophysical research letters*, 29(9):42–1, 2002.

[18] Niklas JT Edberg, M Lester, SWH Cowley, DA Brain, M Fränz, and S Barabash. Magnetosonic mach number effect of the position of the bow shock at mars in comparison to venus. *Journal of Geophysical Research: Space Physics*, 115(A7), 2010.

[19] NJT Edberg, M Lester, SWH Cowley, and AI Eriksson. Statistical analysis of the location of the martian magnetic pileup boundary and bow shock and the influence of crustal magnetic fields. *Journal of Geophysical Research: Space Physics*, 113(A8), 2008.

[20] Ya B Zel'Dovich and Yu P Raizer. *Physics of shock waves and high-temperature hydrodynamic phenomena*. Courier Corporation, 2012.

[21] Gregory G Howes. Laboratory space physics: Investigating the physics of space plasmas in the laboratory. *Physics of Plasmas*, 25(5):055501, 2018.

[22] D Ryutov, RP Drake, J Kane, E Liang, BA Remington, and WM Wood-Vasey. Similarity criteria for the laboratory simulation of supernova hydrodynamics. *The Astrophysical Journal*, 518(2):821, 1999.

[23] DD Ryutov, RP Drake, and BA Remington. Criteria for scaled laboratory simulations of astrophysical mhd phenomena. *The Astrophysical Journal Supplement Series*, 127(2):465, 2000.

doi:10.6844/NCKU201901460

[24] SI Braginskii. Transport processes in a plasma. *Reviews of plasma physics*, 1, 1965.

[25] Alvin Seiff. Recent information on hypersonic flow fields. *NASA Special Publication*, 24:19, 1962.

[26] R. J. Strangeway C. T. Russell, J. G. Luhmann. *Space Physics: An Introduction*. Cambridge University Press, 2016.

[27] John P Verboncoeur. Particle simulation of plasmas: review and advances. *Plasma Physics and Controlled Fusion*, 47(5A):A231, 2005.

[28] Charles K Birdsall and A Bruce Langdon. *Plasma physics via computer simulation*. CRC Press, 2004.

[29] Richard Fitzpatrick. Computational physics. *The University of Texas at Austin*, 2006.

[30] Heiko Burau, Renée Widera, Wolfgang Honig, Guido Juckeland, Alexander Debus, Thomas Kluge, Ulrich Schramm, Tomas E Cowan, Roland Sauerbrey, and Michael Bussmann. Picongpu: a fully relativistic particle-in-cell code for a gpu cluster. *IEEE Transactions on Plasma Science*, 38(10):2831–2839, 2010.

doi:10.6844/NCKU201901460

A Hydrostatic equilibrium

The ionospheric pressure formula Eq. 20 is derived based on hydrostatic equilibrium[1]. The assumption of hydrostatic support is equivalent to assuming that all motion in the ionosphere is static and the equilibrium exists between the gravity and the pressure gradient, i.e.,

$$\frac{dP_i}{dr} = -\rho g, \tag{73}$$

where p is the thermal pressure inside the ionosphere, g is the gravity, ρ is the mass density and r is the radial distance from the center of the planet. Note that the gravity g is assumed to be constant because of the little variation of the value in the whole ionosphere. The pressure can be approximated by the perfect gas law

$$P_i = \frac{\rho}{m} k_B T, \tag{74}$$

where $m = 1.67 \times 10^{-24} g$ is the mass for a singly ionized hydrogen, k_B is Boltzmann's constant and T is the absolute temperature for plasma. Here the temperature T is assumed to be constant. The mass density in Eq. 73 can be eliminated from the introduction of Eq. 74, then the differential equation can be integrated to yield

$$P_i(r) = P_{M,i} \ln\left(-\frac{r - r_{M,i}}{H}\right), \tag{75}$$

where $r_{M,i}$ is the location where peak ionospheric pressure occurs, $P_{M,i}$ is the peak ionospheric pressure, i.e., the thermal pressure at $r_{M,i}$, and H is the scale height of the ionosphere defined as

$$H = \frac{k_B\, T}{m\, g}. \tag{76}$$

doi:10.6844/NCKU201901460

B Rayleigh pitot tube formula

Rayleigh pitot tube formula is used to determine the relation between the thermal pressure before shock and the thermal pressure at the stagnation point in front of the obstacle in section 3.2.1. The rigorous derivation of this formula can be seen in Ref.[5]. We use this formula to get the thermal pressure just outside the ionosphere as a function of the solar wind dynamic pressure. The symbols for the subscripts of the physical quantities used in this section is shown in Fig. 16.

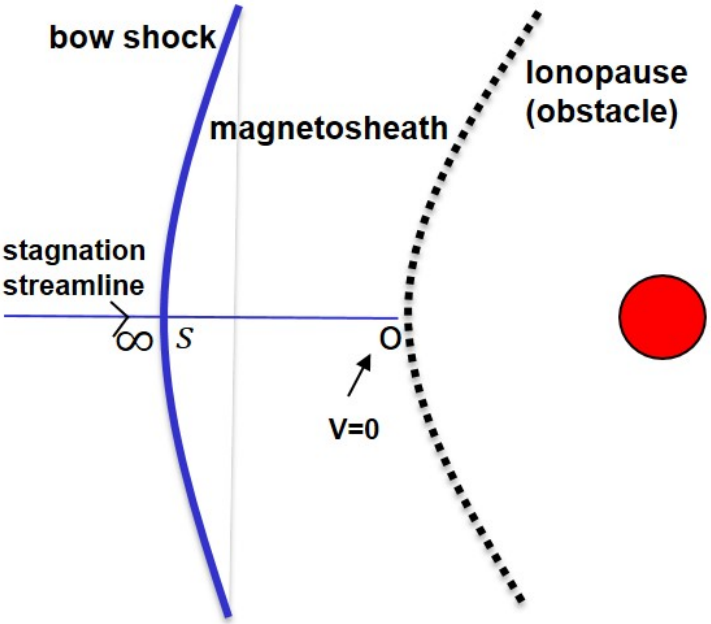

Figure 16: Schematic of the symbols for the subscripts of the physical quantities. “O”, “S”, “∞” stand for the location just outside the obstacle, after shock, before shock.

Rayleigh pitot tube formula can be derived in the following two steps:

1. using the normal shock relation to get the pressure jump relation across shock

$$P_s = \frac{P_\infty}{\gamma+1}\left[2\gamma M_\infty^2 - (\gamma-1)\right], \tag{77}$$

where P_s is the thermal pressure after shock, P_∞ is the thermal pressure before

doi:10.6844/NCKU201901460

shock, i.e., the solar wind thermal pressure, M_∞ is the sonic Mach number of the solar wind and γ is the specific heat ratio, and the thermal pressure after shock to the stagnation point;

2. using Bernoulli's law and adiabatic compression on the stagnation streamline within the magnetosheath to obtain the thermal pressure just outside the ionopause nose

$$P_o = P_s \left[1 + \frac{\gamma - 1}{2} M_s^2 \right]^{\gamma/(\gamma-1)}, \tag{78}$$

where P_o is the thermal pressure just outside the obstacle and M_s is the sonic Mach number after shock.

With the combination of the above two equations and the relation connecting M_s and M_∞, i.e.,

$$M_s^2 = \frac{(\gamma - 1)M_\infty^2 + 2}{2\gamma M_\infty^2 - (\gamma - 1)}, \tag{79}$$

we can obtain the Rayleigh pitot tube formula

$$P_o = P_\infty M_\infty^2 (\frac{\gamma + 1}{2})^{(\gamma+1)/(\gamma-1)} \frac{1}{[\gamma - (\gamma - 1)/(2M_\infty^2)]^{1/(\gamma-1)}}. \tag{80}$$

The detailed derivations of Eq. 77, Eq. 78 and Eq. 79 are in the following paragraphs.

Pressure jump condition across shock There is a discontinuity[5] across the shock front. We consider an element of the shock surface and use a coordinate system fixed to this element with the x-axis representing the normal. The normal shock relation is followed by

$$[\rho v_x] = 0, \tag{81}$$

$$[v_y] = [v_z] = 0, \tag{82}$$

doi:10.6844/NCKU201901460

$$\left[P + \rho v_x^2\right] = 0, \tag{83}$$

$$\left[\frac{1}{2}v_x^2 + \frac{\gamma}{\gamma - 1}\frac{P}{\rho}\right] = 0. \tag{84}$$

Here the brackets mean the difference of the quantity between both sides of the shock discontinuity. Eq. 81 is the continuity of the mass flux, Eq. 82 and Eq. 83 are the continuity of the momentum flux and Eq. 84 is the continuity of the energy flux. To simplify the equation, we set

$$\eta = \frac{\rho_d}{\rho_u} = \frac{v_{ux}}{v_{dx}},\ and\ \xi = \frac{p_d}{p_u}, \tag{85}$$

where the subscript "u" and "d" stand for physical quantities at the upstream and downstream, respectively. Note that the subscript "u" and "d" here is equivalent to the the subscript "∞" and "s" in Eq. 77. Then we rearrange the Eq. 83, we can get

$$(1 - \xi) + \gamma M_u^2 (1 - \frac{1}{\eta}) = 0, \tag{86}$$

where $M_u = v_{ux}/\sqrt{\gamma p_u/\rho_u}$ is the upstream sonic Mach number. Eq. 84 can also be rearranged as

$$\frac{1}{2}M_u^2(1 - \frac{1}{\eta^2}) + \frac{1}{\gamma - 1}(1 - \frac{\xi}{\eta}) = 0. \tag{87}$$

By solving η and ξ from Eq. 86 and Eq. 87, we obtain

$$\eta = \frac{\rho_d}{\rho_u} = \frac{v_{ux}}{v_{dx}} = \frac{(\gamma + 1)M_u^2}{(\gamma - 1)M_u^2 + 2}, \tag{88}$$

and

$$\xi = \frac{p_d}{p_u} = \frac{2\gamma M_u^2 - (\gamma - 1)}{\gamma + 1}. \tag{89}$$

Now we get the Eq. 77.

The relation connecting M_d and $M_u$is

$$
\begin{aligned}
\frac{M_d^2}{M_u^2} &= \frac{\rho_d}{\rho_u}\left(\frac{v_{dx}}{v_{ux}}\right)^2 \frac{P_u}{P_d} && (90)\\
&= \frac{v_{dx}}{v_{ux}}\frac{P_u}{P_d} && (91)\\
&= \frac{(\gamma-1)M_u^2+2}{(\gamma+1)M_u^2} \times \frac{\gamma+1}{2\gamma M_u^2-(\gamma-1)}. && (92)
\end{aligned}
$$

Finally, by simplifying the Eq. 92, we get the Eq. 79.

Pressure variation on the stagnation streamline within magnetosheath Bernoulli equation and adiabatic condition are used to derive the pressure variation after shock. Bernoulli equation for compressible fluid[5] is expressed as

$$\frac{\gamma}{\gamma-1}\frac{P}{\rho}+\frac{1}{2}v^2 = \text{constant along each streamline,} \tag{93}$$

where P is the thermal pressure, ρ is the mass density and γ is the specific heat ratio. By the definition of the sound speed $c = \gamma p/\rho$, Eq. 93 can be written as

$$\frac{c^2}{\gamma-1}+\frac{1}{2}v^2 = \text{constant along each streamline.} \tag{94}$$

According to Bernoulli equation, we can get

$$\frac{c_s^2}{\gamma-1}+\frac{1}{2}v_s^2 = \frac{c_o^2}{\gamma-1}, \tag{95}$$

where subscript “s” and “o” stand for the location after shock and at the obstacle, which is shown in Fig. 16. Also, by $\frac{c_s^2}{c_o^2} = \frac{T_s}{T_o}$ in which T is the temperature, Eq. 95 can be rewritten as

$$\left(\frac{T_s}{T_o}\right)\frac{1}{\gamma-1}+\frac{1}{2}\left(\frac{v_s}{c_o}\right)^2 = \frac{1}{\gamma-1}. \tag{96}$$

Then, we can obtain the relation between T_s and T_o

$$T_s = T_o \left(1 - \frac{\gamma - 1}{2} \left(\frac{v_s}{c_o}\right)^2\right) \tag{97}$$

Now for the purpose of express c_o in terms of c_s, we rearrange the Eq. 95 to obtain

$$c_o^2 = c_s^2 + \frac{1}{2}(\gamma - 1)v_s^2 \tag{98}$$

and substitute Eq. 98 into Eq. 97, then we can get the relation between T_s and T_o in terms of the sonic Mach number after shock M_s

$$T_o = T_s \left(1 + \frac{\gamma - 1}{2} M_s^2\right). \tag{99}$$

By substituting the adiabatic relation

$$\frac{P_o}{P_s} = \left(\frac{T_o}{T_s}\right)^{\gamma/(\gamma-1)} \tag{100}$$

into Eq. 99, we get the Eq. 78.

doi:10.6844/NCKU201901460

C 1D electrostatic particle-in-cell simulation

Particle-in-cell simulations are powerful tools to understand the kinetic behavior behind a complex phenomenon. An 1D PIC code was developed from scratch. It was used to simulate the two-stream instabilities. The details will be explained in this chapter.

C.1 Fundamental of particle-in-cell simulations

Particle-in-cell (PIC) model is a first-principle model providing a kinetic description of a plasma without any physics approximations. It calculates the trajectories of a collection of particles interacting with self-consistent electromagnetic fields. Each computational particle represents a certain number of real particles. The computational cycle of PIC is shown in figure 17[27]. The simulations follow the following steps: (1) Maxwell equations are numerically solved on grids using the particle sources on the discrete grids calculated from the continuous particle locations; (2) the particles are advanced one time step to new momentum and positions by numerically solving the equations of motion. Electromagnetic fields are interpolated from the discrete grid to continuous particle locations; (3) losses or gains of particles at the boundaries are considered; (4) if the model is collisional, Monte Carlo collisions of motion must be considered; (5) the computational loop repeats over step (1) $\sim$(4).

doi:10.6844/NCKU201901460

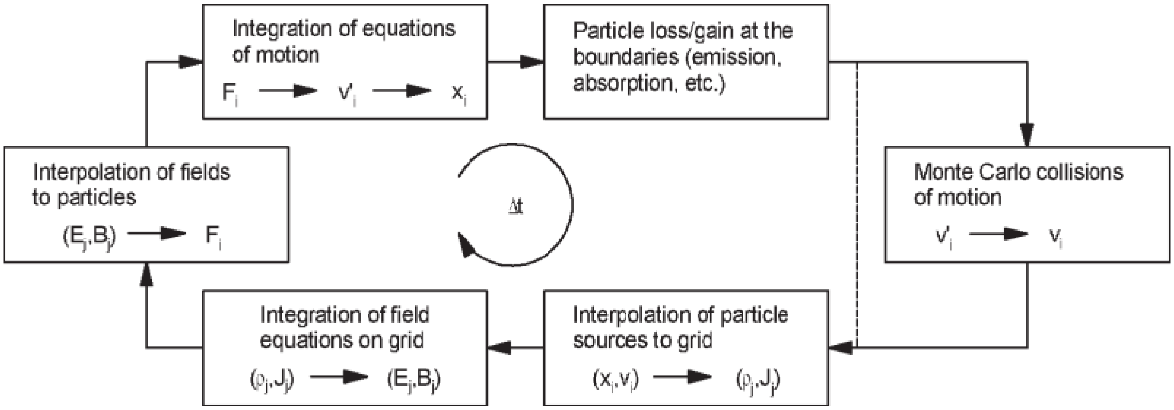

Figure 17: Basic flow loop of PIC simulations.

C.2 My 1D electrostatic particle-in-cell program - two-stream instability

Since a Particle-in-cell program uses many different numerical methods to solve the different equations, e.g. equations of motion and Poisson equation, it must be divided into many subprograms to make the program look clear and easy to be debugged. My main references are "*Plasma physics via computer simulation*"[28] and "*Computational physics*"[29].

C.2.1 Dimensionless equations

Given an uniform, unmagnetized and 1D plasma with N electrons and N unit-charge ions, ions are regarded as static and uniform background since ions are much heavier than electrons. We only consider the motions of electrons. Let $r(i)$ be the position of the i^{th} electron. The equations of motion of the i^{th} electrons is shown as below:

$$\frac{d\,r(i)}{d\,t} = v(i), \tag{101}$$

$$\frac{d\,v(i)}{d\,t} = a(i) = -\frac{e\,E(i)}{m_e}. \tag{102}$$

doi:10.6844/NCKU201901460

where $v(i)$, $a(i)$, $E(i)$, m_e are the velocity of the i^{th} electron, the acceleration of the i^{th} electron, the electric field at the position of the i^{th}electron and the mass of a electron, respectively.

The electric potentials $\phi(x)$ can be obtained from Poisson equation and the electric fields can be expressed in terms of electric potentials:

$$\frac{d^2\,\phi(x)}{d\,x^2} = -\frac{e}{\epsilon_0}\{n_0 - n(x)\}, \tag{103}$$

$$E(x) = -\frac{d\,\phi(x)}{d\,x}, \tag{104}$$

where ϵ_0 is the permittivity of the free space, n_0 is the number density of ions and $n(x)$ is the number density of electrons.

The dominant equations can be simplified via normalization. All the physical quantities is then in the same scale. Variables in the dominant equations are normalized in the following unit (characteristic time, length, potential and field):

$$t_{char} = \omega_p^{-1} = \sqrt{\frac{\epsilon_0\,m_e}{n_0\,e^2}}, \tag{105}$$

$$l_{char} = \lambda_d = \frac{v_{th}}{\omega_p}, \tag{106}$$

$$\phi_{char} = \frac{T_e}{e} = \frac{m_e\,v_{th}^2}{e}, \tag{107}$$

$$E_{char} = \frac{\phi_{char}}{e\lambda_d} = \frac{m_e\,v_{th}^2}{e\lambda_d}, \tag{108}$$

where ω_p is the plasma frequency, λ_d is the Debye length and v_{th}=$\omega_p\,\lambda_d$ is the thermal

doi:10.6844/NCKU201901460

velocity. The normalized dominant equations becomes:

$$\frac{d\,r(i)}{d\,t} = v(i), \tag{109}$$

$$\frac{d\,v(i)}{d\,t} = a(i) = -E(i), \tag{110}$$

$$E(x) = -\frac{d\,\phi(x)}{d\,x}, \tag{111}$$

$$\frac{d^2\,\phi(x)}{d\,x^2} = \frac{n(x)}{n_0} - 1. \tag{112}$$

Periodic boundary condition is used in this program:

$$\phi(0) = \phi(L),\, E(0) = E(L),\, n(0) = n(L). \tag{113}$$

For the two-stream instability, the initial electron distribution function consists of two opposing-propagating Maxwellian beams of beam velocity v_b and thermal spread velocity v_{th}:

$$f(x,v) = \frac{n_0}{2}\left\{\frac{1}{\sqrt{2\,\pi}\,v_{th}} e^{-(v-v_b)^2/2\,v_{th}^2} + \frac{1}{\sqrt{2\,\pi}\,v_{th}} e^{-(v+v_b)^2/2\,v_{th}^2}\right\}. \tag{114}$$

C.2.2 Input parameters

Before running the simulations, we should input parameters. All physical quantities in the dominant equations are normalized by plasma frequency and Debye length. To retrieve the real physics, every physical quantities need to be converted back to real units. The input parameters are shown in the Table 3,4.

doi:10.6844/NCKU201901460

Input parameters	Description
L	Length of simulation system: 0<=x<=L
N	number of electrons
jmax	number of grids
vb	beam velocity
dt	time step
tmax	simulation from 0 to tmax
outputf	output data per outputf

Table 3: Input data for running the simulation.

The size of each grid is defined as: $dx = L/(jmax - 1.)$, and density of ion $dsty0 = N/L$.

Input parameters	Description
wp	plasma frequency
qm	charge/mass
epsi	permittivity
vth	thermal velocity

Table 4: Input data for dealing with the real physics.

Given these parameter values in Table 4, we can get charge q and electron mass me in terms of these real values: $q = wp * wp * epsi/dsty0/qm$ and $me = wp * wp * epsi/dsty0/qm/qm$.

C.2.3 Program overview

The flow chart of my program is shown in Fig. 18. Equations of motion are solved using Leapfrog method. Poisson equation is solved using Gauss-Seidal method. The program is initiated to satisfy Leapfrog method by pushing $v(t = 0)$ back to $v(t = -\frac{dt}{2})$. Initial locations of the particles are randomly distributed; Initial velocities of the particles satisfy double-peak Gaussian distribution as Eq. 114. Then it can run the PIC loop until the end of the simulation. The computer language I use is FORTRAN and post-processing software is MATHEMATICA.

doi:10.6844/NCKU201901460

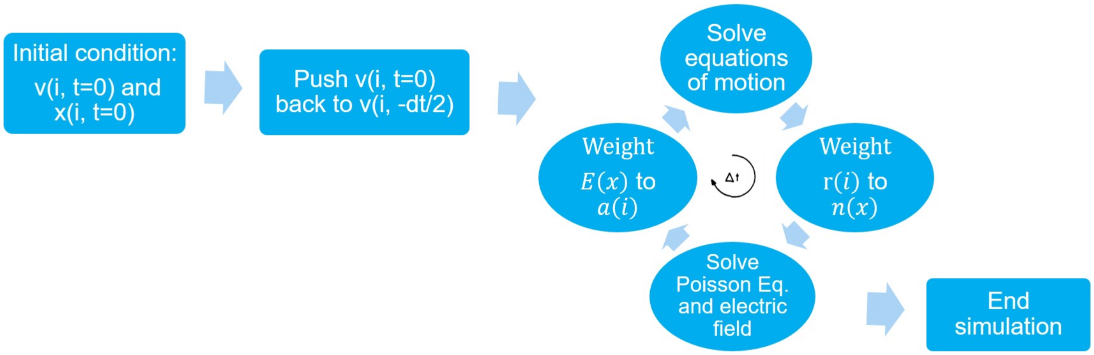

Figure 18: Flow chart of my 1D electrostatic PIC program.

C.2.4 Leapfrog method for solving equations of motion

Leapfrog method, one of the methods to solve ODE using the second-order center difference scheme is used. It requires only few operations and storage since the update can be done in place immediately. Equations of motion are discretized as below:

$$v_{new} = v_{old} + a_{old}\, dt, \tag{115}$$

$$r_{new} = r_{old} + v_{new}\, dt. \tag{116}$$

In Leapfrog method, velocity is in multiples of integers plus one half time step. However, location and acceleration (force) are in multiple of integer time step (shown in Fig. 19[28]). Something should be noticed here: first, the program should be initiated by pushing $v(t=0)$ back to $v(t=-\frac{dt}{2})$ using the force at t=0; second, the energy calculated from locations and velocities must be adjusted to the same time.

doi:10.6844/NCKU201901460

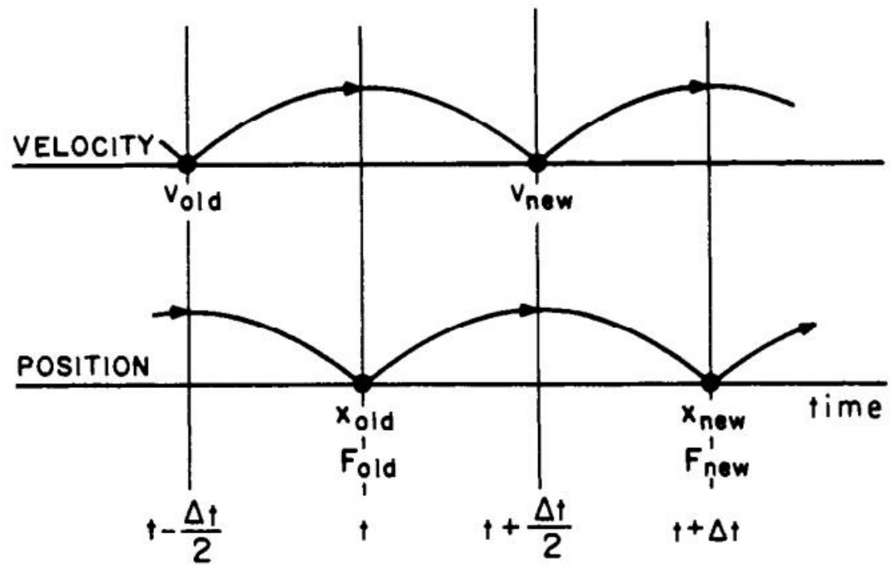

Figure 19: Schematic of the velocity and location flow of Leapfrog method.

Benchmark To verify the program is correct, the numerical results are compared to the calculation results for $dt = 1$, $N = 5$, $r(i) = i + 7$, $v(i) = 2$, $a(i) = 1$, $L = 10$ with periodic boundary condition. The results after 1 time step are shown in Table 5.

$r(i)$	$[v_{new}(i) + v_{old}(i)]/2$
1	2.5
2	2.5
3	2.5
4	2.5
5	2.5

Table 5: The simulation results after 1 time step.

C.2.5 Gauss-Seidel method for solving Poisson equation

To solve Poisson equation numerically, it is first discretized and then rearranged into matrix form. Gauss-Seidel method, one of the iterative methods for solving matrix, is used. The discretized electric field is defined as

$$E(j) = \frac{\phi(j-1) - \phi(j+1)}{2\,dx}. \tag{117}$$

Benchmark To benchmark, the electric field and electric potential for one proton located at $x = 5$ (length of system $L = 10$) and $dx = 0.001$ are calculated. Periodic boundary condition is used. The simulation result is shown in Fig.20. The simulation results are consistent with the analytic solution and satisfy periodic boundary condition.

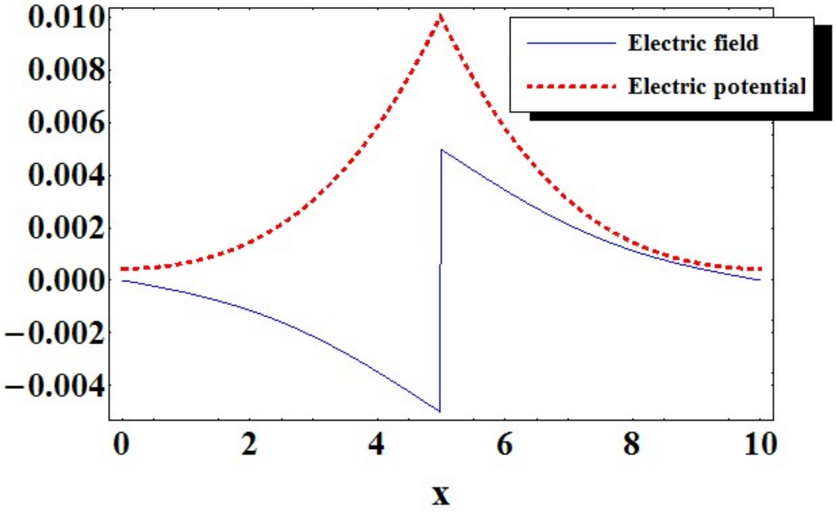

Figure 20: The simulation results when one proton is at the middle of the system using periodic boundary condition.

C.2.6 Linear weighting method for connecting particles and grids

1. Density

Density is evaluated by locations of particles using linear weighting method. For $x(j) <$

doi:10.6844/NCKU201901460

$r(i) < x(j+1)$, we let

$$n(j) \rightarrow n(j) + \left[\frac{x(j+1) - r(i)}{dx}\right] / dx, \tag{118}$$

$$n(j+1) \rightarrow n(j+1) + \left[\frac{r(i) - x(j)}{dx}\right] / dx. \tag{119}$$

Benchmark Our code of linear weighting method is benchmarked using the example as shown in the Figure 21. When a particle is located at $r = 0.5$, the neighboring grids at $x = 0$ and $x = 1$ are both incremented by 0.5. In the same manner, when a particle is located at $r = 4.8$, the neighboring grids at $x = 4$ and $x = 5$ are incremented by 0.2 and 0.8, respectively.

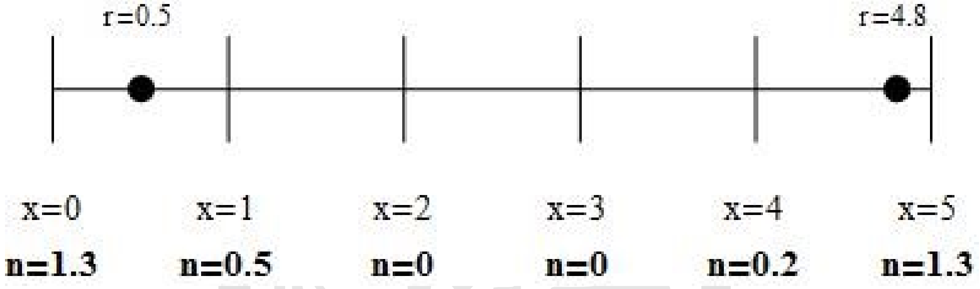

Figure 21: Benchmark of Density subprogram. Locations of electrons are input and densities are output.

2. Acceleration

Acceleration of each particles is evaluated by electric field at each grids using linear interpolation and the normalized equations of motion (Eq. 110). Linear interpolation of electric field is defined as

$$E(i) = \left[\frac{x(j+1) - r(i)}{dx}\right] E(j) + \left[\frac{r(i) - x(j)}{dx}\right] E(j+1). \tag{120}$$

Benchmark Our code of evaluating acceleration is benchmarked using the example as shown in the Figure 22. In this example, the values of the electric field are same as the values of the grid locations. When a particle is located at $r = 1.5$, electric field at this particle location is 1.5 due to the linear interpolation. In the same manner, when a particle is located at $r = 4.8$, electric field at this particle location is 4.8. Then, according to the equation 110, electric fields at particle locations 1.5 and 4.8 are -1.5 and -4.8, respectively.

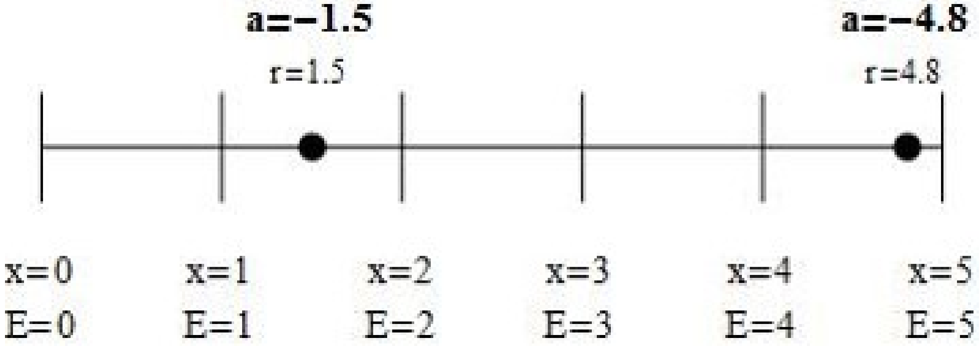

Figure 22: Benchmark of Acceleration. Locations of electrons and Electric field at grids are input; acceleration at electrons is output.

C.3 Two-stream instability: selected results and analysis

The input parameters are: $N = 20000$, $jmax = 1001$, $L = 100.$, $dt = 0.1$, $tmax = 50.1$, $outputf = 2.5$, $wp = 1$, $qm = 1$, $vth = 1$, $epsi = 1$. The following results and analysis are based on these input parameters.

Fig. 23 shows the phase space plots at different times. There are 20000 dots representing 20000 movable electrons in each figure. Initially, the locations of electrons are randomly distributed but velocities follow the double-peak Maxwellian distribution (Eq. 114). As time goes on, the plasma becomes unstable and instability grows. When t=20 and 30, we observe some vortices. It means at that time some particles are oscillating or trapped in the local area.

doi:10.6844/NCKU201901460

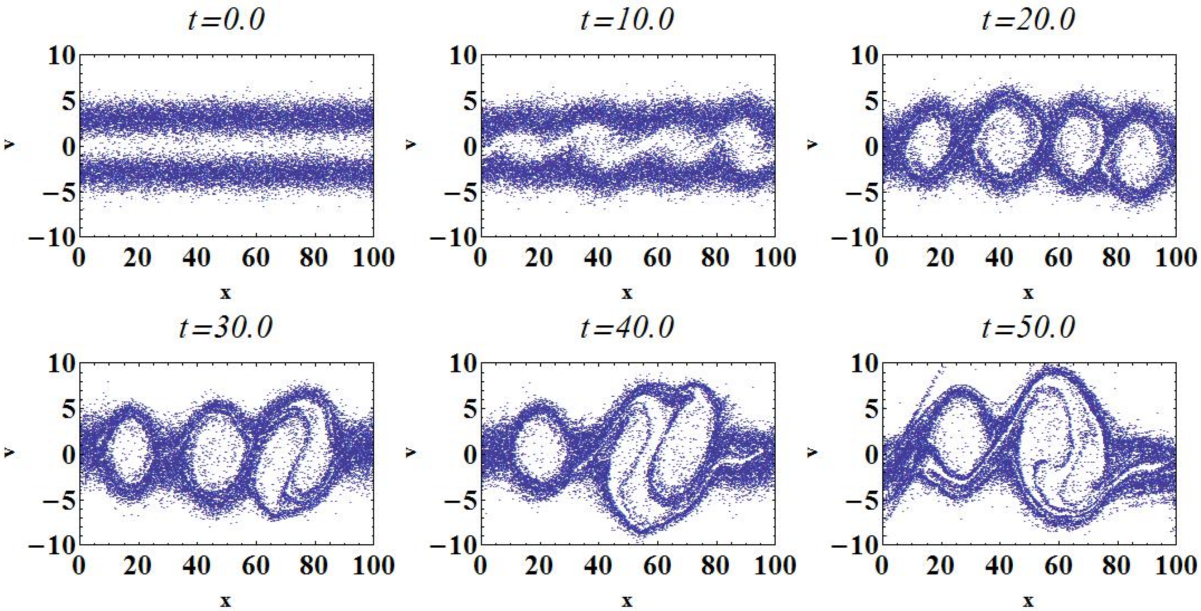

Figure 23: The phase space plots of the two-stream instability with 20000 movable electrons and 20000 fixed background ions at different time.

Fig. 24 shows the plots of electric fields at different time. Initially since the ions electrons are uniformly distributed, the electric fields are almost zero everywhere. As time goes on, the electric fields are no longer zero everywhere due to the instability. At t=20, the particles are uniformly trapped in the four islands as shown in Fig. 23, so the electric field versus location is like a sine function. The instability gradually grows so that the electric field also increases as time goes on.

doi:10.6844/NCKU201901460

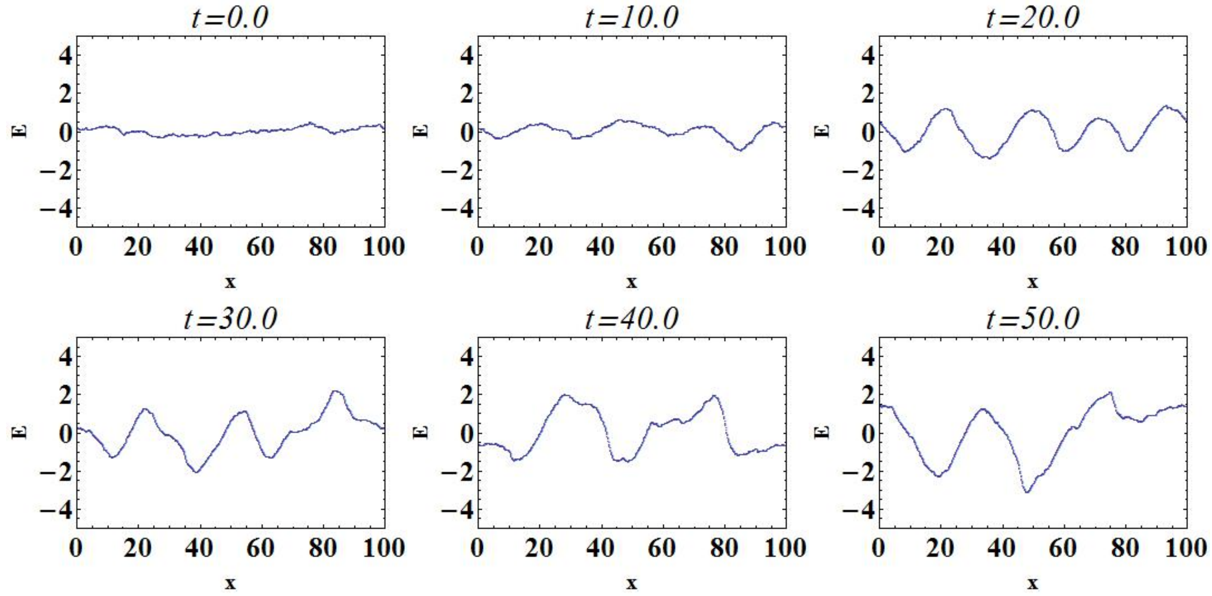

Figure 24: Plots of Electric fields at different time.

Fig. 25 shows the phase space trajectories with different initial velocities. To understand the motion of each electrons, electrons with different initial velocities are traced in phase space. For electrons with high initial velocity (∼5), they are unbounded. However, for those with low initial velocity (∼0), they are trapped in islands and have the oscillating motions.

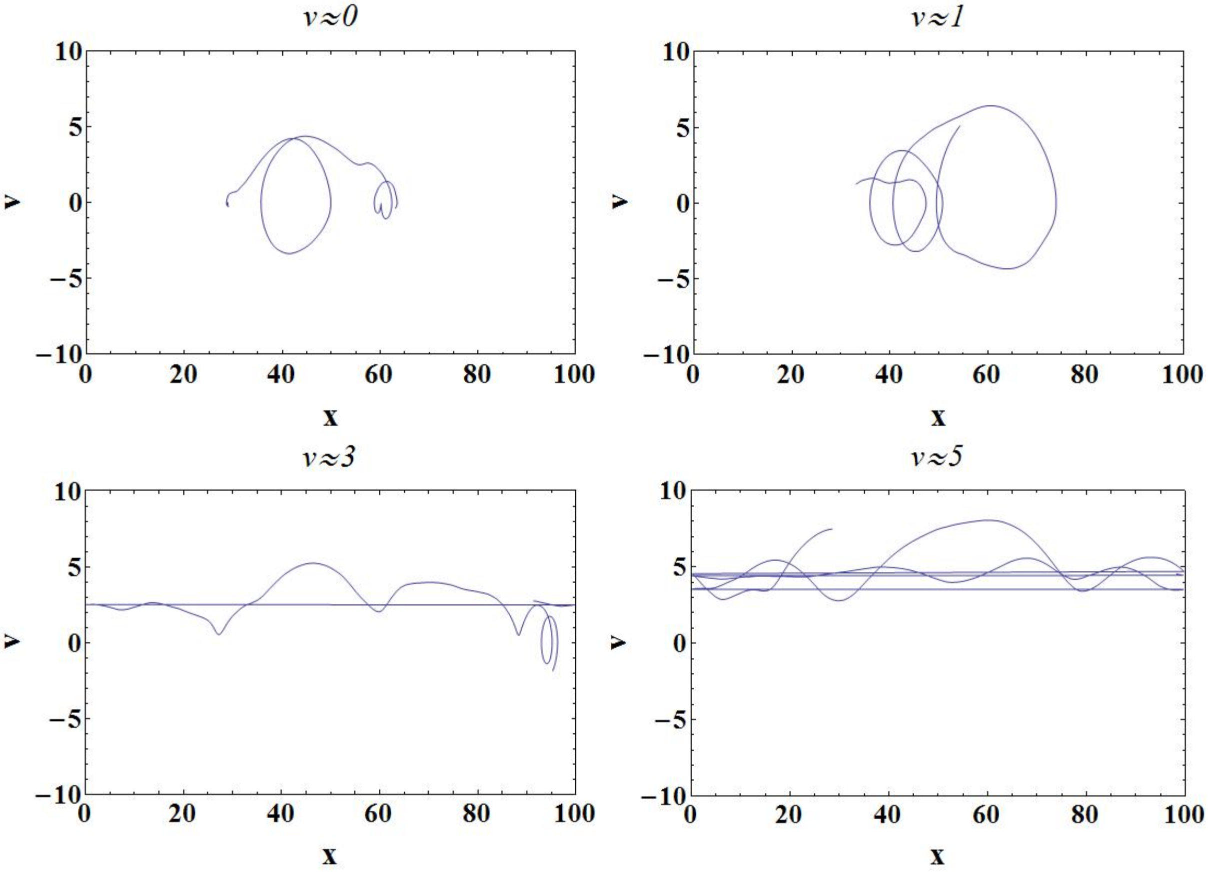

Figure 25: Phase space trajectories of particles with different initial velocities. Particles with different initial velocity either are trapped or unbounded.

Fig. 26 shows the velocity distribution at different time. Initially, velocities follow the double-peak Maxwellian distribution (Eq. 114). As the time goes on, the instability grows so that double-peak Maxwellian distribution are destroyed. The distribution gradually merge and the velocities spread broader.

doi:10.6844/NCKU201901460

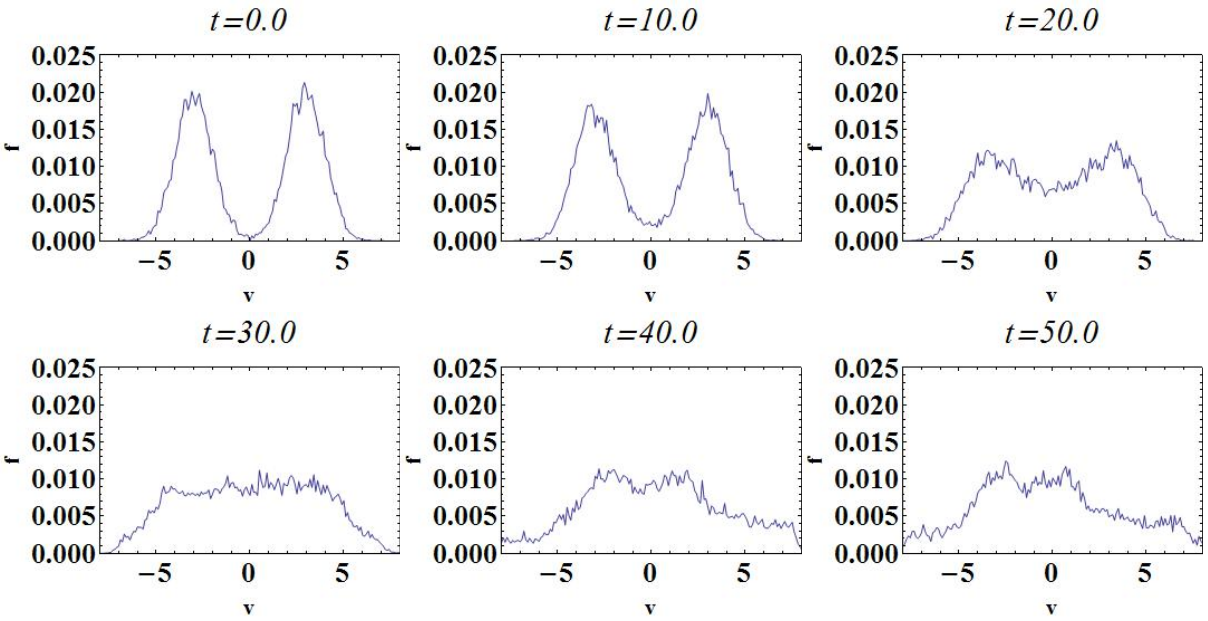

Figure 26: Velocity distribution at different time.

Fig. 27 shows the total energy and electrostatic energy varies with time. Total energy and electrostatic energy are defined as

$$E_{total} = \sum_{i=1}^{N} \frac{1}{2}\, m_e\, v_i^2 + \sum_{j=1}^{jmax} \frac{1}{2}\, \epsilon_0\, E_j^2 dx, \tag{121}$$

$$E_{electric} = \sum_{j=1}^{jmax} \frac{1}{2}\, \epsilon_0\, E_j^2 dx. \tag{122}$$

The energy does not conserve because our simulation does not satisfy courant conditioin that $v\, dt \leq dx$. The timestep in my simulation should be smaller after t=10.

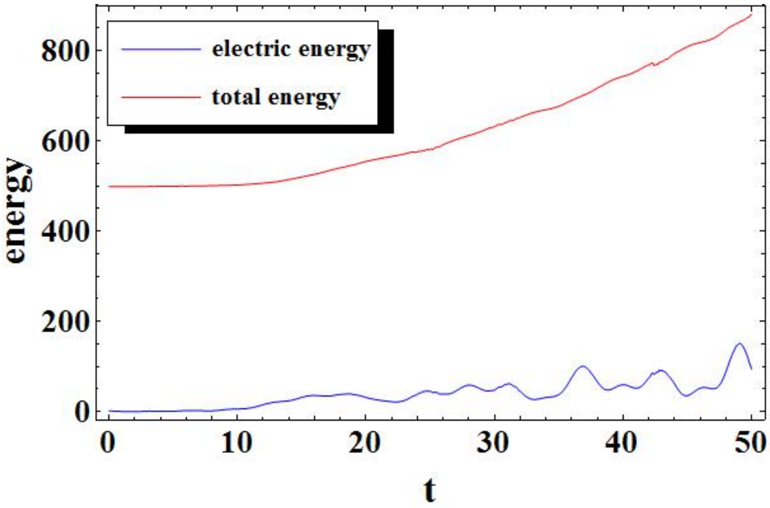

Figure 27: Total energy and electrostatic energy as a function of time.

C.4 Comparison withe the linear theory

For two stream instability of cold plasma, the dispersion relation can be obtained from both kinetic theory and fluid theory. The initial distribution function is

$$f_0(v) = \frac{1}{2} n_o [\delta(v - v_0) + \delta(v + v_0))]. \tag{123}$$

We can obtain the dispersion relation from inserting Eq. 123 into the linearized Vlasov equation. The dispersion relation is

$$\omega^2 = k^2\, v_0^2 + \frac{1}{2}\omega_{pe}^2 \left(1 \pm \sqrt{1 + \frac{8k^2 v_0^2}{\omega_{pe}^2}} \right). \tag{124}$$

So we can get the growth rate ω_{im} as

$$\frac{\omega_{im}}{\omega_{pe}} = \sqrt{-\left[\frac{k^2 v_0^2}{\omega_{pe}^2} + \frac{1}{2}\left(1 - \sqrt{1 + \frac{8k^2 v_0^2}{\omega_{pe}^2}} \right) \right]}. \tag{125}$$

doi:10.6844/NCKU201901460

The comparison of the simulation results with the linear theory is shown in Fig.28.

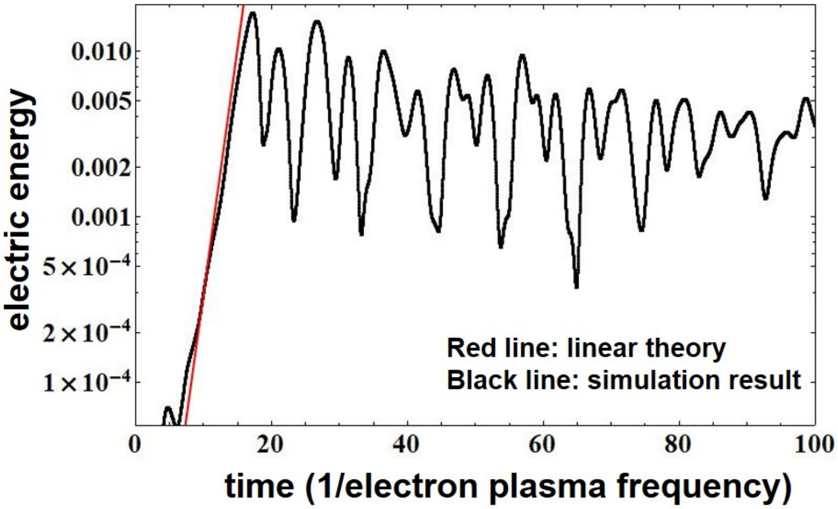

Figure 28: The electric energy against the time: the comparison of the simulation results with the linear theory. Here $k\,v_o = 0.5$.

doi:10.6844/NCKU201901460

D Setup of the code "PIConGPU" on our cluster

The code PIConGPU[30], which is 3D electromagnetic particle-in-cell code will GPU parallelization, has been installed on our cluster. We built the computer in Ubuntu operation system and installed two graphic cards from scratch. The graphic card NVIDIA GTX 1060 is used. We bought the graphic cards through 佳欣科技. *picongpu.profile-dev* is the script I wrote for setting up the environment for running PIConGPU. The following is the usage of executing the example of PIConGPU in our computer:

Use *spack* (a tool for setting the environment) to load all dependent libraries, then add the directory of PIConGPU code to environment variables

1. `. picongpu.profile-dev` or `source picongpu.profile-dev`
2. `pic-create $PIC_EXAMPLES/LaserWakefield $HOME/picInputs-dev/myLWFA`
3. `cd ~/picInputs/myLWFA`
4. `pic-build`
5. `tbg -s bash -c etc/picongpu/0001gpus.cfg -t etc/picongpu/bash/mpirun.tpl $HOME/runs-dev/lwfa_002`

doi:10.6844/NCKU201901460